nature physics

Article

https://doi.org/10.1038/s41567-023-02223-z

Laser ablation and fluid flows reveal the mechanism behind spindle and centrosome positioning

Received: 3 February 2022

Accepted: 23 August 2023

Published online: 02 November 2023

Check for updates

Hai-Yin Wu[1,2] ✉, Gökberk Kabacaoğlu[3], Ehssan Nazockdast[3,4], Huan-Cheng Chang[5], Michael J. Shelley[3,6] & Daniel J. Needleman[2,3,7]

Few techniques are available for studying the nature of forces that drive subcellular dynamics. Here we develop two complementary ones. The first is femtosecond stereotactic laser ablation, which rapidly creates complex cuts of subcellular structures and enables precise dissection of when, where and in what direction forces are generated. The second is an assessment of subcellular fluid flows by comparison of direct flow measurements using microinjected fluorescent nanodiamonds with large-scale fluid-structure simulations of different force transduction models. We apply these techniques to study spindle and centrosome positioning in early *Caenorhabditis elegans* embryos and to probe the contributions of microtubule pushing, cytoplasmic pulling and cortical pulling upon centrosomal microtubules. Based on our results, we construct a biophysical model to explain the dynamics of centrosomes. We demonstrate that cortical pulling forces provide a general explanation for many behaviours mediated by centrosomes, including pronuclear migration and centration, rotation, metaphase spindle positioning, asymmetric spindle elongation and spindle oscillations. This work establishes methodologies for disentangling the forces responsible for cell biological phenomena.

The movement and positioning of centrosomes, microtubule (MT) organizing centres, govern many important phenomena in cell biology, including the orientation and positioning of the spindle[1–8], the position of the nucleus[9–11] and the migration of pronuclei[12,13]. Centrosomes display three basic behaviours in various systems: (1) directed motion[7,12–15], (2) stable positioning[7,16,17] and (3) oscillations[18–20]. All of these behaviours are observed in early *Caenorhabditis elegans* embryos. The pronuclear complex (PNC) undergoes directed motion to the cell centre with its two centrosomes becoming aligned with the embryo's long axis[14]. The spindle then forms between the two centrosomes and is stably positioned in the cell centre[16]. Finally, as the spindle elongates and is positioned asymmetrically, it and its centrosomes undergo transverse oscillations[14,19,21–24]. It is poorly understood how these different behaviours arise from the underlying mechanical and biochemical processes, although extensive work demonstrates the importance of astral MTs[25–29] that radiate outward from the centrosomes and of the molecular motor dynein[30–37].

All movements in cells result from forces. Due to the small size of the centrosomes (<10 μm), their slow speeds (<1 μm s^{-1}) and the viscous nature of the cytoplasm (>100 mPa s), the Reynolds number associated

[1]Department of Physics, Harvard University, Cambridge, MA, USA. [2]Department of Molecular and Cellular Biology, Harvard University, Cambridge, MA, USA. [3]Center for Computational Biology, Flatiron Institute, Simons Foundation, New York, NY, USA. [4]Department of Applied Physical Sciences, University of North Carolina, Chapel Hill, NC, USA. [5]Institute of Atomic and Molecular Sciences, Academia Sinica, Taipei, Taiwan. [6]Courant Institute of Mathematical Sciences, New York University, New York, NY, USA. [7]John A. Paulson School of Engineering and Applied Sciences, Harvard University, Cambridge, MA, USA. ✉e-mail: hywu@g.harvard.edu

with their motion is $Re < 10^{-7} \ll 1$. Thus, inertial forces are negligible in comparison to viscous forces. Consequently, the velocity of a centrosome is proportional to the forces acting upon it. Thus, a central challenge is to identify the origin of those forces yielding these distinct behaviours of centrosomes (that is directed motions, stable positioning and oscillations). Most proposals centre around three possible types of forces acting through astral MTs: MTs pushing on the cortex, MTs pulled by force generators anchored to the cortex and MTs pulled by force generators in the cytoplasm[38].

Here, we develop biophysical approaches to unambiguously determine the extent to which different centrosome motions in one-cell *Caenorhabditis elegans* embryos are driven by MT pushing or pulling, and if pulling, whether it is of cortical or cytoplasmic origin. This relies on several advances. First, we developed and utilized femtosecond stereotactic laser ablation (FESLA) as a versatile tool for dissecting when, where and in what direction forces originate. From our ablation studies, we conclude that pulling forces dominate during PNC migration and rotation, spindle centring, elongation and oscillations. Second, at all these stages, we compared subcellular flow measurements using microinjected fluorescent nanodiamonds (FNDs) with large-scale fluid dynamics simulations of flows resulting from pulling forces on astral MTs, from either force generators residing on the cortex or in the cytoplasm. The simulations of the former showed remarkable agreement with flow measurements, whereas those of the latter were profoundly different. This supports the hypothesis of pulling originating from the cortex, while also demonstrating that subcellular flows can encode in their structure a powerful signature of the mechanical basis of force generation. Finally, we constructed a coarse-grained theory, amenable to analysis, for centrosome motion that directly relates the biophysical properties of MT nucleation, growth and interaction with cortical force generators to the cell biological behaviour of centrosomes. This theory demonstrates that cortical pulling alone is sufficient to explain centrosome behaviours. Taken together, our results argue that cortical pulling forces provide a unifying explanation of the diverse centrosome motions—directed, stable positioning and oscillations—found in *C. elegans* embryos. Given the ubiquity of these centrosome behaviours across cell biology and the proposed role of cortical pulling forces in many different contexts, the investigative framework presented here should be widely applicable.

Pulling forces drive spindle oscillations

We began by studying the transverse oscillations of the first mitotic spindle in the late metaphase to the anaphase in *C. elegans* embryos (Fig. 1a and Extended Data Fig. 1a). We used spinning-disc confocal microscopy to image GFP::β-tubulin and mCherry::γ-tubulin, and tracked the motion of the spindle poles using automated image analysis (Methods and Extended Data Fig. 1b–g). As others have noted, the anterior pole (Fig. 1a,b, orange) and the posterior pole (Fig. 1a,b, blue) oscillate out of phase with each other (Supplementary Video 1), with the posterior pole displaying larger amplitudes and more robust oscillations[21,22].

To investigate how astral MTs contribute to these motions, we utilized a new FESLA system capable of cutting three-dimensional (3D) patterns with highly controlled timing and location (Fig. 1c and Methods)[39,40]. FESLA utilizes a reduced-repetition-rate ultrafast femtosecond laser to produce highly localized cuts with submicrometre precision[41–45]. We sought to determine the relative contribution of the pushing and pulling forces to spindle oscillations by selectively cutting different populations of astral MTs. If a centrosome is being pushed from the rear, then cutting the astral MTs behind the centrosome will cause the oscillations to stop (Fig. 1d, left). Similarly, if a centrosome is being pulled forward, then cutting astral MTs in the front will halt its motion (Fig. 1d, right). We first used this approach to explore the forces acting on centrosomes when they are at the midpoint of their oscillation, moving with maximum speed (Fig. 1b, inset, T_m). When astral MTs in front of these centrosomes were cut, the centrosomes immediately stopped moving along their original course (Fig. 1e, Supplementary Video 2 and Extended Data Fig. 2d), indicating that this forward movement was primarily driven by pulling from these astral MTs. The centrosomes subsequently moved in the opposite direction, suggesting that pulling forces are also exerted by the astral MTs at the rear of the centrosome. Cutting astral MTs at the rear of the centrosome during this same point in the oscillations only marginally impacted their velocity (Fig. 1f, Supplementary Video 2 and Extended Data Fig. 2d), suggesting that the downward pulling forces greatly dominate over upward pulling forces (Fig. 1g).

We next investigated the forces at the peak of the oscillation, when their velocity is zero (Fig. 1b, inset, T_p). Cutting the astral MTs below the centrosome that faced the distant cortex inhibited the downward motion that occurs subsequent to this time in control embryos (Fig. 1h, Supplementary Video 2 and Extended Data Fig. 2d), indicating that the downward movement in control embryos is primarily driven by pulling from these astral MTs. The centrosomes subsequently moved in the opposite direction, suggesting that pulling forces are also exerted by the astral MTs above the centrosome. Cutting the astral MTs above the centrosome during this same point in the oscillation did not significantly impact the centrosomes subsequent returning motion (Fig. 1i, Supplementary Video 2 and Extended Data Fig. 2d). Taken together, these results indicate that, at the peaks of the oscillations, astral MTs exert net pulling forces on centrosomes. Since the centrosome has zero velocity at this point, the pulling forces from above and below the centrosome must be equal and opposite (Fig. 1j).

We next made cuts in the shape of an open cylinder around the posterior centrosome with the cylinder axis aligned with the transverse (y) axis (Fig. 2a), thereby severing the MTs perpendicular to the direction of oscillation (Fig. 2b,c, and Supplementary Video 3). The centrosomes continued to oscillate after cutting (Fig. 2d), with significant increases in amplitude immediately afterward (Fig. 2e and Extended Data Fig. 2g,h). We also observed oscillations after double (y–z) plane cuts made in the MTs in two planes orthogonal to the spindle axis, which left the perpendicular MTs of the remaining two planes intact (Extended Data Fig. 2e,h). Since the centrosomes still reversed direction after these cuts, this result demonstrates that the bending of MTs perpendicular to the oscillation axis[46] is not required for the restoring mechanism of the oscillations. It is possible that substantial pulling and pushing forces can simultaneously be exerted by different astral MTs located on the same side of the centrosome. To test this, we made cup-shape cuts to temporarily eliminate all MTs around centrosomes except for those extending to one transverse side (Fig. 2f,g). We observed that the centrosome rapidly moved very close to the cortex (Fig. 2h and Supplementary Video 3) after a cup cut, approaching a minimum distance of 5.3 ± 0.3 μm from the cortex, compared to 9.7 ± 0.2 μm in uncut embryos (Fig. 2i). Thus, pulling forces dominate over pushing forces from astral MTs on the same side of a centrosome. Furthermore, the observation that centrosomes approach very close to the cortices after cup cuts suggests that pushing forces do not substantially contribute to the restoring force during normal oscillations.

Cortical pulling forces drive spindle oscillations

We next investigated whether the pulling forces that act on centrosomes during transverse oscillations result from force generators in the cytoplasm (such as from dynein transporting organelles along MTs[47–50]) or on the cell cortex[2,14,30,35,37,51–56] (such as cortically anchored dynein or MT depolymerizers). Subcellular fluid flows provide a means to distinguish between these possibilities because cytoplasmically based pulling forces tend to produce flows in the direction opposite to MT motions, whereas cortically based pulling forces tend to produce flows in the same direction as MT motions (Fig. 3a).

We first simulated the effect of cytoplasmic forces generated by dynein transporting cargo along MTs at time T_m (Fig. 1b, inset), which produced complex, 3D flows, consisting of multiple vortices (Fig. 3b,

https://doi.org/10.1038/s41567-023-02223-z

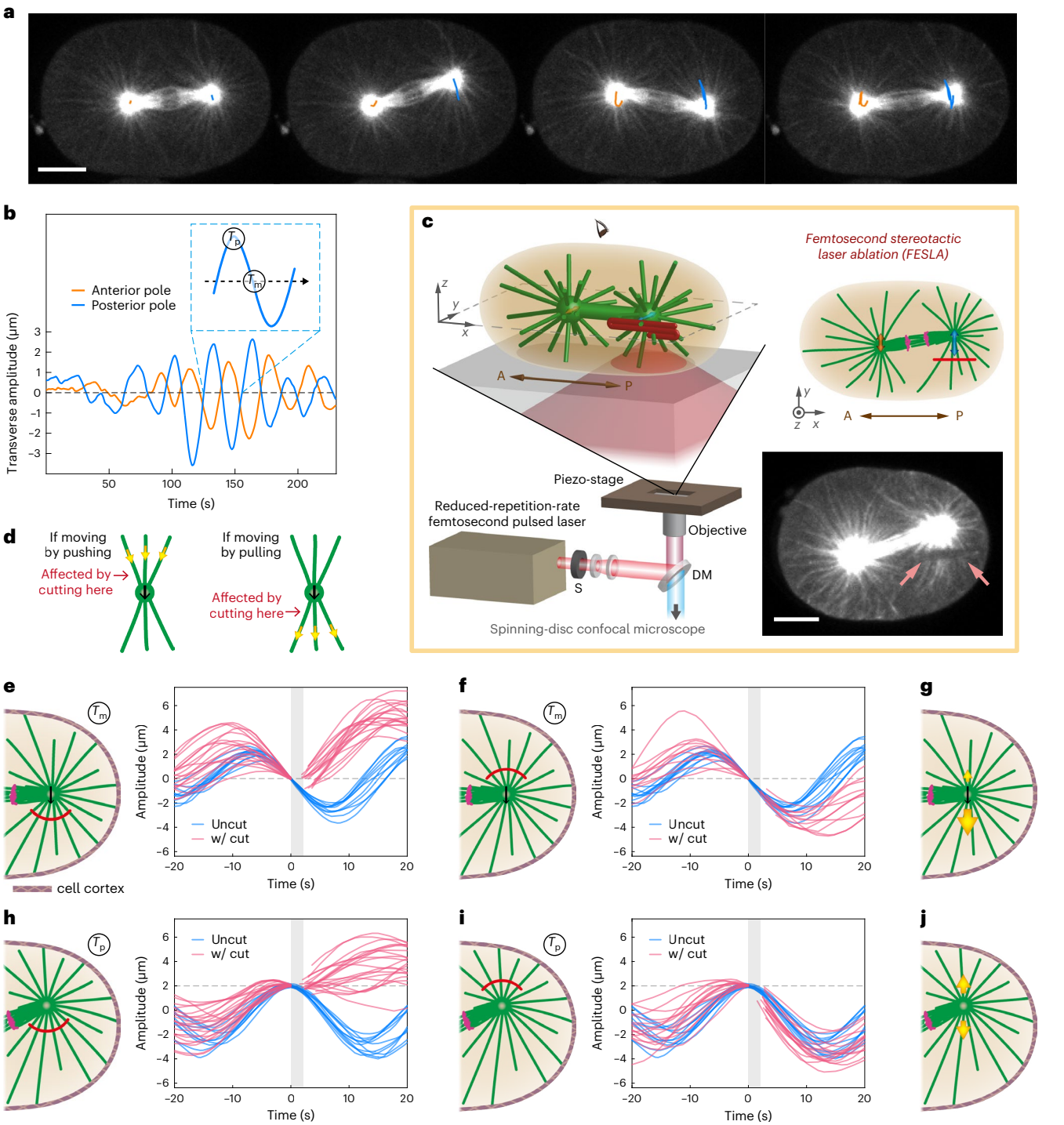

Fig. 1 | Laser ablation during spindle oscillations in the first mitotic division of *C. elegans*. **a**,**b**, Spindle oscillations in a one-cell *C. elegans* embryo labelled with GFP::β-tubulin. **a**, One oscillation cycle and the corresponding trajectories of the anterior (orange) and posterior (blue) centrosomes (scale bar, 10 μm). **b**, Transverse amplitudes of the centrosomes and the definition of times T_p and T_m. **c**, FESLA. Left, the foci of a Ti:sapphire femtosecond pulsed laser with a reduced repetition rate (16–80 kHz) were scanned over the sample in a complex 3D pattern (red line) for ablation using a three-axis piezo-stage (MTs are in green; long brown arrow, the A–P axis; A, anterior; P, posterior; S, shutter; DM, dichroic mirror). Right, upper, 2D view of the *x*–*y* imaging plane (magenta, chromosomes; orange arrow, motion of the anterior centrosome; blue arrow, motion of the posterior centrosome). Right, lower, image of a sample after ablation. Arrows indicate the cut region (scale bar, 10 μm). **d**, Illustration of how cutting at different locations can distinguish between pushing and pulling scenarios. **e**–**j**, Arc-shaped cuts made in astral MTs on either transverse side of the posterior centrosomes at two different time points in the oscillation cycle. At time T_m (**e**–**g**), the arc cuts in front of the centrosomes (**e**) and at the rear of the centrosomes (**f**) give the proposed net forces (yellow arrows) (**g**). At time T_p (**h**–**j**), the arc cuts below the centrosomes (**h**) and above the centrosomes (**i**) give the proposed net forces (**j**). See Extended Data Fig. 2b,c for the quantification: $\Delta v_y = v_{y(\text{after})} - v_{y(\text{before})}$. All statistical results are displayed in Extended Data Fig. 2d and presented as mean ± standard error of the mean (SEM) as follows. At time T_m (**e**,**f**), $\Delta v_y = 0.05 \pm 0.05\ \mu m\ s^{-1}$ in 11 uncut embryos (control). **e**, $\Delta v_y = 0.86 \pm 0.06\ \mu m\ s^{-1}$ in 18 arc-cut embryos with $P = 5.0 \times 10^{-10}$. **f**, $\Delta v_y = -0.06 \pm 0.04\ \mu m\ s^{-1}$ in 11 arc-cut embryos with $P = 0.087$. At time T_p (**h**,**i**), $\Delta v_y = -0.55 \pm 0.04\ \mu m\ s^{-1}$ in 11 uncut embryos (control). **h**, $\Delta v_y = 0.18 \pm 0.05\ \mu m\ s^{-1}$ in 21 arc-cut embryos with $P = 5.8 \times 10^{-10}$. **i**, $\Delta v_y = -0.61 \pm 0.04\ \mu m\ s^{-1}$ in 16 arc-cut embryos with $P = 0.28$. The *P* values were calculated by two-tailed Student's *t*-tests based on the corresponding uncut and arc-cut data sets. See Extended Data Fig. 2a for the FESLA dimensions. w/cut, with cut.

https://doi.org/10.1038/s41567-023-02223-z

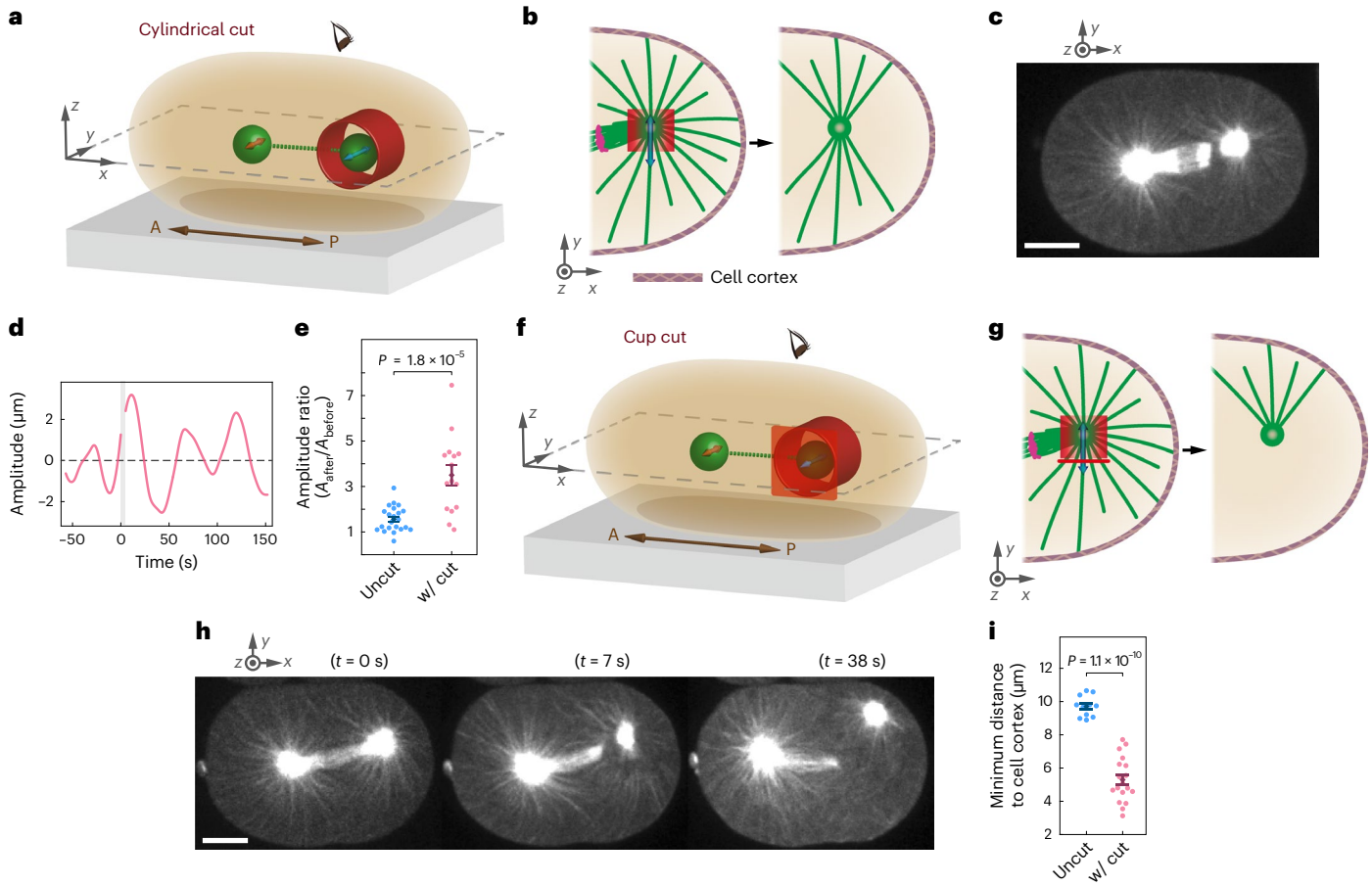

Fig. 2 | Open-cylindrical and cup cuts around the posterior centrosomes during spindle oscillations. Spindle poles are illustrated by green balls connected with green dashed lines in the 3D schematics **a** and **f**. The posterior portions of the *x*–*y* midplanes (view from the top) are shown in the corresponding 2D schematics **b** and **g**, with spindles and astral MTs in green and chromosomes in magenta. The ablation geometry is portrayed in red in all schematics. **a**–**e**, Open-cylindrical cuts. **a**, 3D schematic of a cut aligned along the transverse oscillation (*y*) axis. **b**, 2D schematic showing the ablation of the MTs perpendicular to the oscillations, which leaves the transverse astral MTs intact. **c**, An image taken directly after an open-cylindrical cut (scale bar, 10 μm). **d**, Example of oscillation amplitudes before and after the cut, with the time of ablation marked by the light grey vertical strip. **e**, The amplitudes of the oscillations increased after open-cylindrical cuts were made. See Extended Data Fig. 2g for the quantification of the amplitude ratio. $A_{after}/A_{before} = 1.6 \pm 0.1$ in 22 uncut cycles, and $A_{after}/A_{before} = 3.5 \pm 0.4$ in 15 embryos with open-cylindrical cuts. **f**–**i**, Cup cuts. **f**, 3D schematic of a cut with opening facing in the transverse direction. **g**, 2D schematic showing the ablation of all astral MTs except those extending out from the opening of the cup. **h**, Images before and after a cup cut (scale bar, 10 μm). **i**, Comparison of the minimum distances from the approaching posterior centrosomes to the cell cortices, between uncut (9.7 ± 0.2 μm, $n = 11$) and cup-cut (5.3 ± 0.3 μm, $n = 18$) embryos. See Extended Data Fig. 2j for the distance measurement. See Extended Data Fig. 2f,i for the FESLA dimensions. All data are presented as mean ± SEM, and the *P* values were calculated using two-tailed Student's *t*-tests (error bars, SEM).

top). To help visualize these flows, we projected and averaged the flows in the two-dimensional (2D) plane of spindle motion (Fig. 3b, bottom). This flow pattern occurs because cytoplasmic pulling forces tend to create minus-end directed flows along MTs, but fluid incompressibility prevents these flows from being uniformly directed inward towards centrosomes. A very different pattern of flow is produced by simulating cortical pulling forces, as seen in both 3D (Fig. 3c, top) and 2D projections (Fig. 3c, bottom). In this case, the downward motion of the posterior centrosome leads to an overall rotational flow, with a much smaller, counterrotating backflow between the posterior centrosome and the cortex (Fig. 3c, bottom inset).

With these predictions in hand, we next experimentally measured cytoplasmic fluid flows in *C. elegans* embryos during spindle oscillations. We microinjected passivated[57,58] FNDs[59–64] into *C. elegans* syncytial gonads, which subsequently became incorporated into embryos (Methods). We imaged the FNDs and the spindle, labelled with green fluorescent protein (GFP)::β-tubulin, with 3D time-lapse spinning-disc confocal microscopy (Fig. 3d and Supplementary Video 4). We tracked the FNDs in 3D using automated image analysis (Fig. 3d, right) and averaged the 2D projection of the FND trajectories from multiple embryos and multiple oscillations (Extended Data Fig. 3a,b and Methods). Figure 3e shows the resulting measured fluid flow throughout the embryo when the centrosomes are at the midpoint of their oscillations (T_m). The measured fluid flow remarkably resembles that calculated from the cortical pulling model (compare Fig. 3c with Fig. 3e), displaying both the characteristic circular motions around the two spindle poles as well as the subtler counterrotating backflows between the posterior centrosomes and the cortices (see the insets in Fig. 3c,e). If both cytoplasmic and cortical pulling forces were present, then the resulting flows, and centrosome velocities, would be a linear combination of those shown in Fig. 3b,c (Supplementary Methods). Since, within experimental error, the measured flow agrees with the pattern observed in simulations of cortical pulling, with no sign of the complex flows predicted from cytoplasmic pulling, we estimate that the contributions from cortical pulling forces are manyfold greater than those from cytoplasmic pulling forces. Moreover, averaging the fluid flows at the peak of the oscillation (T_p) revealed no coherent fluid motions, in agreement with simulations for cortical

https://doi.org/10.1038/s41567-023-02223-z

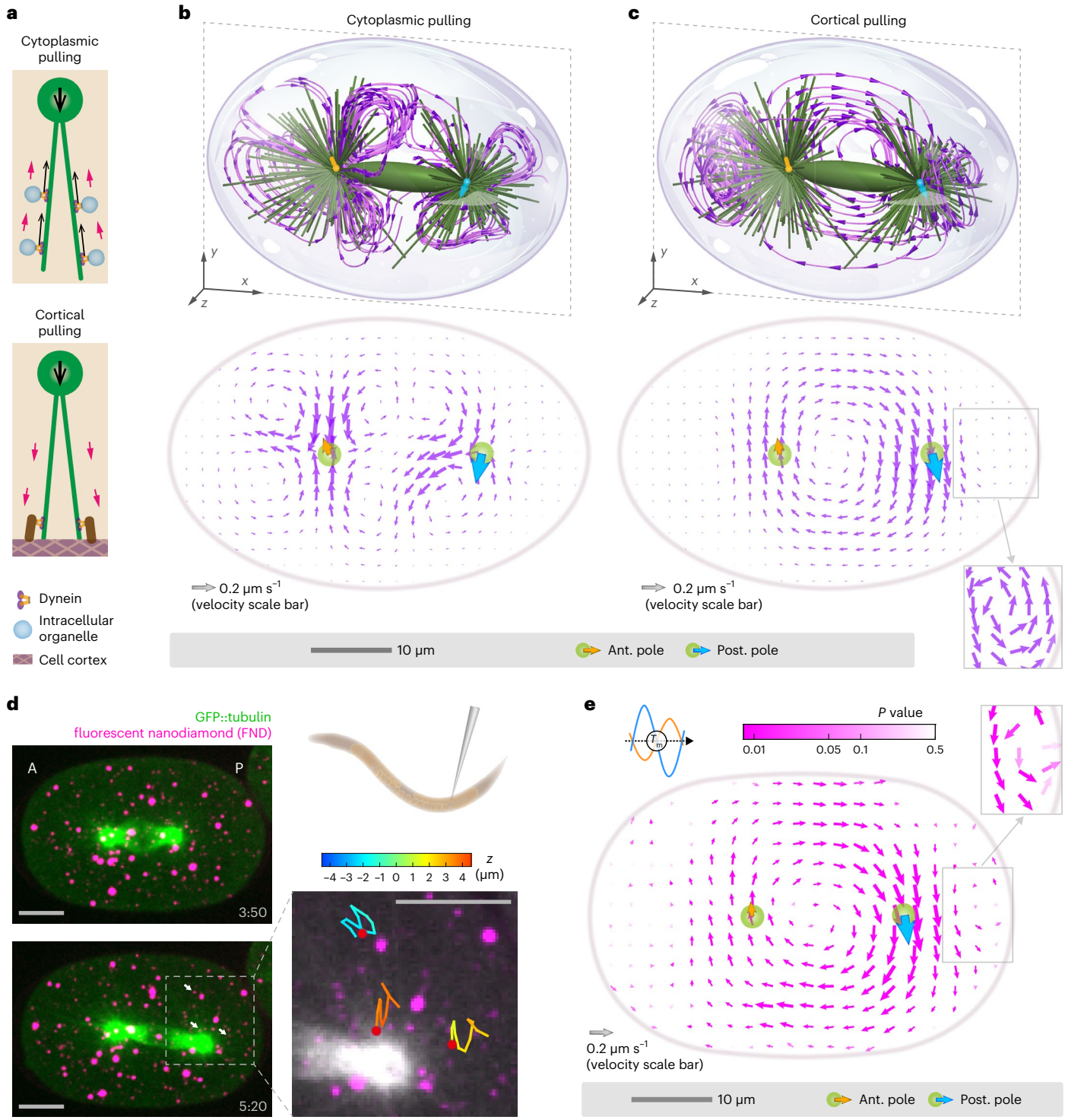

Fig. 3 | Fluid flows during spindle oscillations. a, Schematic of fluid flow directions near a centrosome (green circle) and astral MTs (green lines). Top, in a cytoplasmic pulling model, the direction of fluid flow (magenta arrows) is opposite to that of centrosome motion (bold black arrow). Bottom, in a cortical pulling model, fluid flow and centrosome motion are in the same direction. **b**,**c**, Top panels, 3D computational fluid dynamics simulations near the midpoint of the oscillations at time T_m with cytoplasmic pulling (**b**) or cortical pulling (**c**). Bottom panels, averaged projections of the fluid vector fields onto the x–y planes of spindle motion from the above simulations. **d**, Left panels, two time frames ($\Delta t = 90$ s) of the maximal intensity projection of z-stack images with microinjected FNDs. Right, enlargement of the illustrative 50 s 3D trajectories of FNDs (the three from the left image pointed out by white arrows), with their end locations marked by red dots. The z positions of the 3D trajectories are indicated by the colour bar. (All scale bars in **d** are 10 μm.) **e**, Experimentally measured fluid flow vector field near the oscillation midpoint at time T_m obtained by tracking FNDs from 20 embryos and averaging their projected x–y velocities. The length of the arrows is proportional to the flow velocity, and the colour indicates the statistical significance of the flow speed (P-value colour bar) (see Methods for details). Arrows on centrosomes indicate the mean measured centrosome velocities. The enlargements of the backflows in **c** and **e** are displayed with fixed-length vectors. Ant., anterior; Post., posterior.

pulling forces at that point in the oscillations and in strong disagreement with simulations for cytoplasmic pulling forces (Extended Data Fig. 3d–f). In sum, these results strongly suggest that the pulling forces acting on centrosomes during spindle oscillations are predominately cortically based.

Cortical pulling positions in prometaphase and metaphase spindles

During the first mitotic division of *C. elegans* (Supplementary Video 1), the spindle forms near the cell centre and is aligned along the cell's long axis. The spindle remains centred in the prometaphase and the early metaphase, and slowly elongates towards the posterior in the late metaphase. We next investigated the nature of the forces acting on the spindle at these times.

We first used FESLA to test whether astral MTs exert pushing or pulling forces on the spindle when it is stably centred. Ablating rectangular planes either below (x–z plane rectangular cuts, Fig. 4a) or posterior (y–z rectangular cuts, Fig. 4b) to the posterior centrosomes caused the centrosomes to immediately displace away from the cuts, suggesting that astral MTs in both directions exerted net pulling forces on the centrosomes (Supplementary Video 5). We next performed cups cuts, as described above, leaving only a cone of astral MTs associated with the centrosome emanating in either the transverse (Fig. 4c) or longitudinal (Fig. 4d) directions. In both cases, the centrosomes rapidly moved in the direction of the remaining astral MTs, displacing farther than in response to plane cuts and only slowing down once the astral MTs in the ablated regions had begun to recover (Supplementary Video 5). Thus, these experiments provide no sign of MT pushing forces, even when the centrosomes are displaced by ~5 µm towards the cell cortices, suggesting that pushing made a minimal contribution to the positioning forces near the cell centre (longer MTs push more weakly[65]).

We next used a combination of large-scale fluid dynamics simulations and measurements of fluid flow to determine whether the pulling forces that stably centre the spindle originate in the cytoplasm or at the cortex. Simulations of cytoplasmic pulling display extensive flows organized into vortices (Fig. 4e). Such large flows are necessarily present in a cytoplasmic pulling model, even when the spindle is stationary, as they are ultimately responsible for the forces that maintain the spindle position in this model. In contrast, flows only result from the motion of the spindle in a cortical pulling model, so are absent when the spindle is stationary (Fig. 4f). To experimentally measure the fluid flow when the spindle displayed no appreciable motion in the prometaphase, we tracked FNDs and averaged their trajectories together (Methods). No coherent fluid motion was present (Fig. 4g), consistent with the prediction of the cortical pulling model and inconsistent with cytoplasmic pulling.

We next investigated fluid flow during the slow spindle elongation in the metaphase when the posterior centrosome moves and the anterior centrosome is mostly stationary, before the onset of spindle oscillations. Simulations of the cytoplasmic pulling model (Fig. 4h) and cortical pulling model (Fig. 4i) produced distinct flows. Experimentally, averaging the trajectories of FNDs during spindle elongation in the metaphase (Methods) resulted in a flow pattern quite like the prediction of the cortical pulling model but inconsistent with the cytoplasmic pulling model (Fig. 4j). Since, within experimental error, the measured flow agrees with the pattern observed in simulations of cortical pulling, we estimate that the contributions to velocities from cortical pulling forces are manyfold greater than those from cytoplasmic pulling forces.

Taken together, through FESLA and by comparing fluid flow measurements with large-scale fluid dynamics simulations, we demonstrated that spindle positioning in the prometaphase and metaphase is primarily driven by cortical pulling forces, rather than from MT pushing or cytoplasmic pulling.

Cortical pulling drives pronuclear centration and rotation

At an even earlier stage (Supplementary Video 1), the female and male pronuclei meet near the posterior cortex, and the PNC migrates towards the cell centre. During the centration process, the PNC rotates to align with the long axis of the cell[66]. We next investigated the nature of the forces acting on the PNC.

We first used FESLA to test whether astral MTs exert pushing or pulling forces on the PNC. We separately probed astral MTs associated with the leading or trailing centrosomes by ablating rectangular planes near the centrosomes outside the pronuclei (Fig. 5a and Supplementary Video 6). In both cases, the centrosomes rapidly moved away from the cut astral MTs (Extended Data Fig. 4f,g), which is clearly seen by realigning the centrosomes relative to the cuts (Fig. 5b). These results imply that astral MTs primarily exert pulling forces on centrosomes during pronuclear centration. Simulations of cytoplasmic pulling during pronuclear rotation and centration produce a complex pattern of flows (Fig. 5c). In contrast, in both cortical pulling simulations (Fig. 5d and the inset) and FND-based measurements (Fig. 5e and the inset), the fluid rotates in conjunction with the PNC and contains a subtle backflow near the posterior centrosome.

Fluid flow measurements support cortical pulling but not cytoplasmic pulling. However, the MTs connecting the PNC to the anterior cortex cannot be clearly visualized[48], and such MTs are necessary to support cortical pulling during pronuclear centration. We performed an additional test by cutting a large semicircular arc in front of the migrating PNC, close to the anterior cortex, such that only MTs a few micrometres away from the cortex would be ablated (Fig. 5f,g). The PNC immediately ceased advancing after the cutting (Fig. 5h and Supplementary Video 6), indicating that centration requires astral MTs to contact the anterior cortex. This result is not easily explained by a cytoplasmic pulling model but would be expected in a cortical pulling model. In sum, through FESLA and fluid flow analysis, we demonstrated that PNC migration is primarily driven by cortical pulling forces.

Cortical pulling as an explanation for centrosome behaviours

Our above work shows that pulling forces always locally dominate (from FESLA) and these pulling forces result from cortical force generators (by comparing fluid flow measurements with large-scale fluid dynamics simulations) at all times in one-cell *C. elegans* embryos, namely during anaphase spindle oscillations, during metaphase and prometaphase stable positioning and during PNC centration. We next investigated whether cortical pulling forces alone are sufficient to account for these diverse centrosome motions. We developed a coarse-grained model derived from the biophysics of MT nucleation, growth and interaction with pulling cortical force generators (Supplementary Notes). In this model (Fig. 6a), a centrosome nucleates MTs at a rate γ, which grow from their plus-end with velocity V_g and undergo a catastrophe[46,52] (that is, a switch from growing to shrinking) with rate λ. MTs that hit an unoccupied force generator bind to it and experience a pulling force f_0, which is transmitted to the centrosome. The force generators are stoichiometric. Each force generator can bind to at most one MT at a time[39]. Bound MTs detach from force generators at a rate κ, whereupon they undergo a catastrophe. MTs that hit the cell cortex without binding to a force generator undergo an immediate catastrophe. As in Fig. 6b, we consider a single centrosome moving along the y axis in a spherical cell of radius W, uniformly covered with M cortical force generators[21,22,24,30,36,46,51,67]. The net pulling force on the centrosome is the sum of pulling forces on all its MTs. This net pulling force is balanced by a drag force proportional to the centrosome's velocity (Supplementary Notes).

We first tested this model to see whether it is able to account for spindle oscillations. We numerically simulated the model using realistic parameters (Extended Data Table 1 and Extended Data Fig. 5)

https://doi.org/10.1038/s41567-023-02223-z

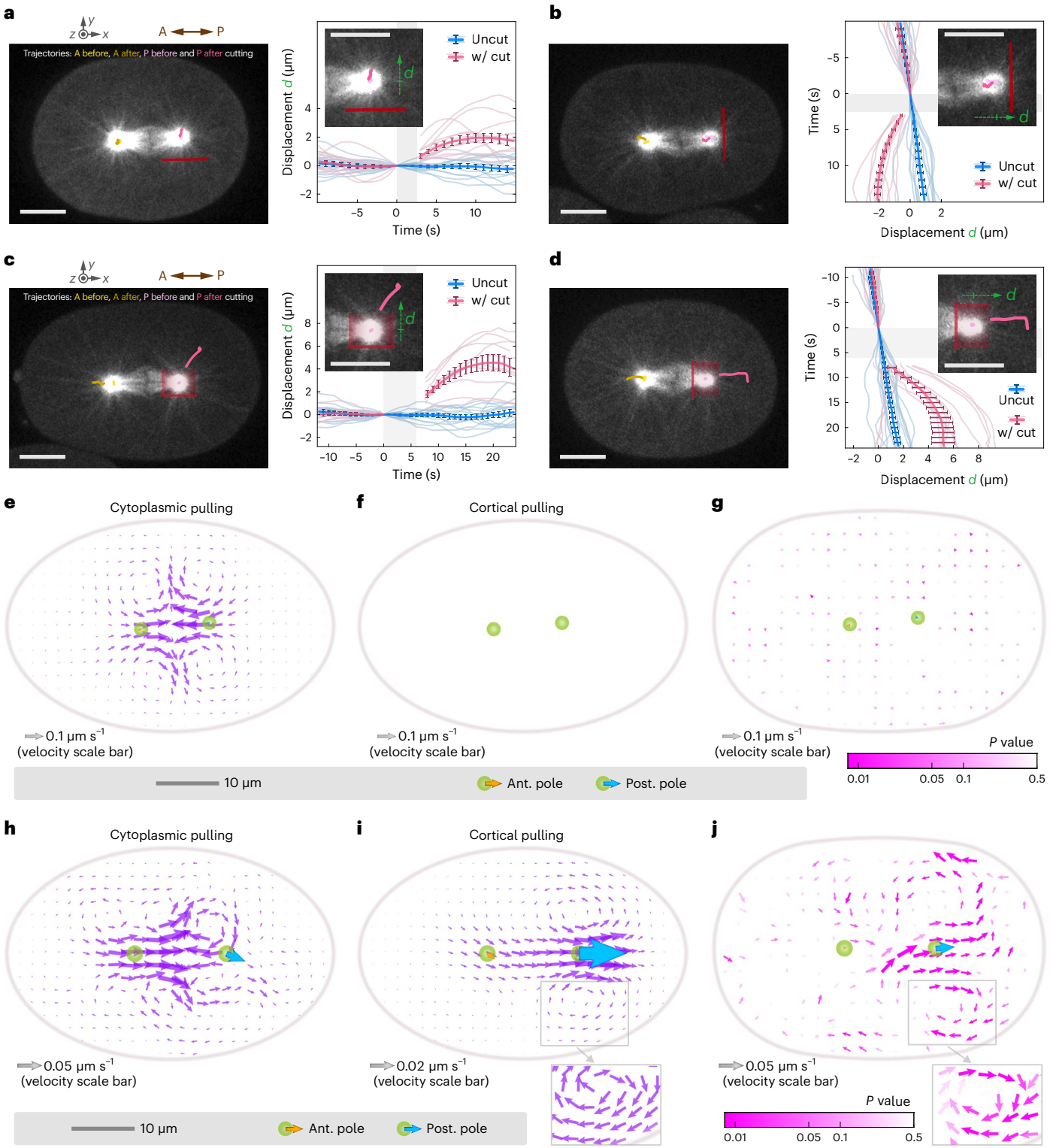

Fig. 4 | Laser ablation and fluid flows in prometaphase and metaphase. **a**–**d**, Laser ablation performed in metaphase (cutting patterns in red). The centrosome trajectories before and after cutting are plotted on the images with the designated colours. Right panels illustrate the corresponding definition of the displacement *d* in their insets and show the centrosome displacement data for uncut and cut embryos, with the mean value curves and SEM error bars overlaying the semitransparent raw data curves. All scale bars on images, including those of insets, are 10 μm. **a**, Rectangular (*x*–*z*) plane cuts on the transverse sides of the posterior centrosomes. **b**, Rectangular (*y*–*z*) plane cuts located posteriorly to the posterior centrosomes. **c**,**d**, Cup cuts surrounding the posterior centrosomes with the opening mouths facing the transverse sides (**c**) or the posterior ends (**d**). See Extended Data Fig. 4a–d for the FESLA dimensions. Sample numbers are **a**, $n = 14$ (uncut), $n = 14$ (with cut); **b**, $n = 14$ (uncut), $n = 13$ (with cut); **c**, $n = 14$ (uncut), $n = 10$ (with cut) and **d**, $n = 14$ (uncut), $n = 14$ (with cut). **e**,**f**, Simulated fluid flows in prometaphase under (**e**) the cytoplasmic pulling or (**f**) the cortical pulling models. **g**, The flow vector field of averaged experimental results from tracking FNDs in nine embryos in prometaphase. **h**,**i**, Simulated fluid flows during spindle elongation in metaphase under (**h**) the cytoplasmic pulling or (**i**) the cortical pulling models. **j**, Experimental flow vector field derived from averaging the movements of tracked FNDs in 14 embryos during spindle elongation in metaphase. The highlighted backflows in the enlargements in **i** and **j** are plotted with fixed-length vectors. The statistical significance of the velocity vectors is indicated by their colour scale (*P*-value colour bar) in **g** and **j**.

https://doi.org/10.1038/s41567-023-02223-z

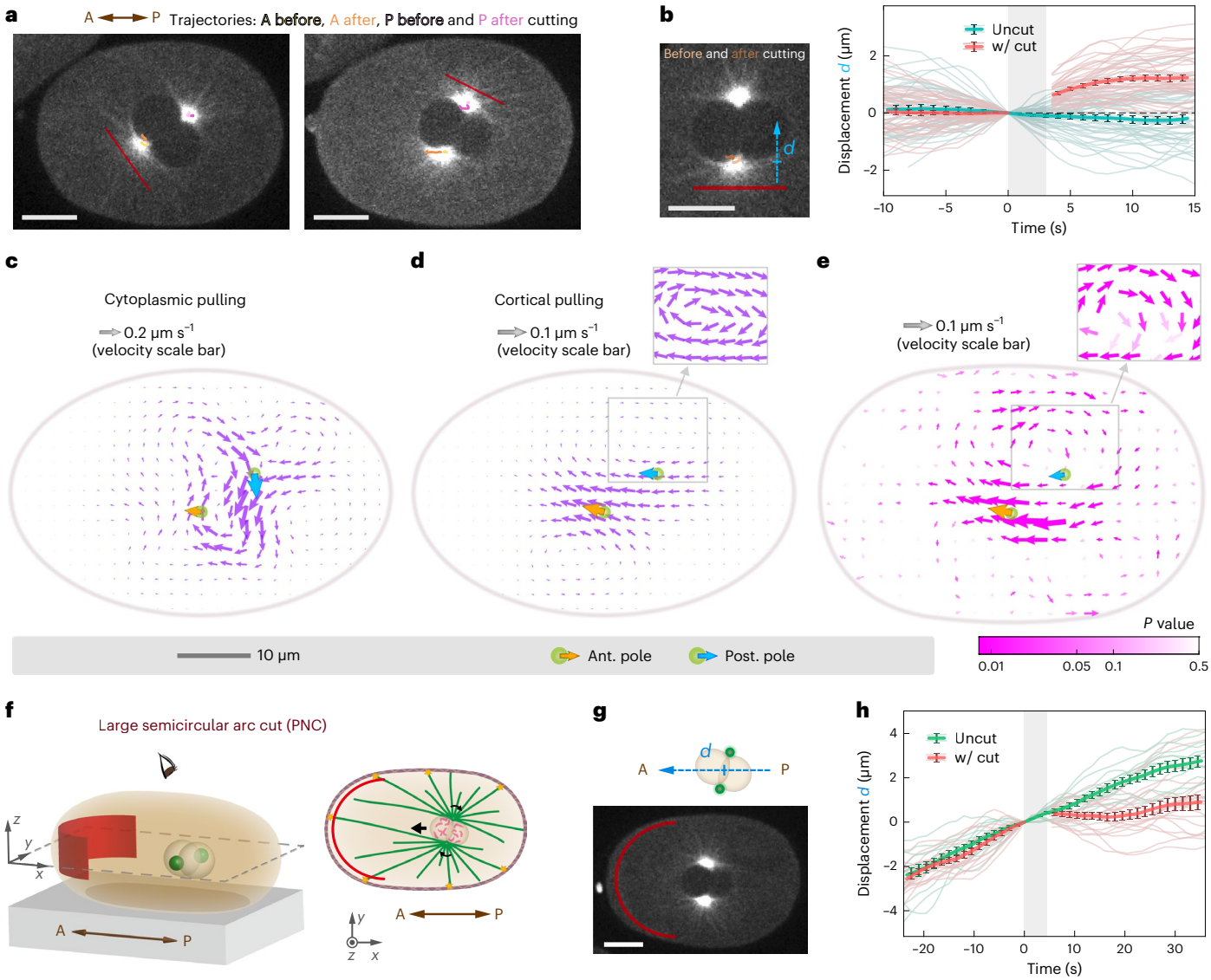

Fig. 5 | Laser ablation and fluid flows during migration of the PNC. **a**,**b**, Rectangular plane cuts (ablation drawn in red) during PNC migration. **a**, Images indicating the locations of plane cuts. Left, cutting near the anterior or leading centrosome. Right, cutting near the posterior or trailing one. In both images, the centrosome trajectories within a window from 10 s before to 15 s after cutting are plotted. **b**, Left, the definition of the centrosome displacement d, which is the relative orthogonal (away from the cut) displacement from the locus right before cutting. Right, uncut ($n = 48$) and cut ($n = 48$) displacement data sets. **c**,**d**, Simulated fluid flows under (**c**) the cytoplasmic pulling or (**d**) the cortical pulling models. **e**, Experimental flow vector field obtained from averaging eight embryos with tracked FNDs. The statistical significance of the velocity vectors is indicated by their colour scale (P-value colour bar). **f**–**h**, Large semicircular arc cuts close to the anterior cortices during PNC migration. **f**, 3D schematic (left) and 2D schematic (right) of the arc cut (drawn in red). The black arrows on the 2D schematic indicate PNC translation and rotation. **g**, An image taken right after a semicircular arc cut. To quantify the progression of PNC migration, the displacement d is calculated by projecting the PNC centre onto the embryo long axis. **h**, Migration displacements of uncut ($n = 14$) and cut ($n = 19$) embryos. For each ablated embryo, the zero point ($d = 0$) is defined by the PNC location right before cutting. All scale bars on images are 10 μm. See Extended Data Fig. 4e,h for the FESLA dimensions. All displacement data are presented with mean value curves and SEM error bars overlaying the semitransparent raw data curves. In the enlargements in **d** and **e**, the highlighted circular flow patterns are displayed with fixed-length vectors.

during the anaphase and found that the centrosome oscillates with a similar amplitude and frequency to those seen experimentally (Fig. 6c). When the centrosome is at the top of the oscillations (Fig. 6d, t_1), MTs are attached to force generators directly above the centrosome whereas force generators directly below the centrosome are largely unoccupied. MTs then start to attach to force generators below the centrosome, causing it to start moving downward (Fig. 6d, t_2). More MTs continue to attach to the lower side and detach from the upper side (Fig. 6d, t_3), and eventually, the process reverses (Fig. 6d, t_4).

We gained further insights into the mechanism of oscillations from a linear stability analysis. A centrosome at the centre can lose stability to an oscillatory state via a Hopf bifurcation if there is more than a critical number of cortical force generators, given by:

$$M_c = \frac{3\eta\bar{\Omega}}{f_0\bar{P}^2}\frac{V_g W}{(\kappa W - 2V_g)}$$

where the steady-state rate of impingement of MTs onto force generators for a stationary centrosome at the cell centre before the start of oscillations is $\bar{\Omega} \approx \frac{\gamma}{4}\left(\frac{r}{W}\right)^2 \exp(-W\lambda/V_g)$, η is the centrosome drag coefficient (including the associated astral MT array) and r is the capture radius of a force generator (which includes the distance over which a MT explores the cortex before binding). Here, $\bar{P} = \bar{\Omega}/(\bar{\Omega} + \kappa)$

is the steady-state probability of a force generator being bound (Supplementary Notes). In this model, oscillations are only possible if $\frac{1}{\kappa} < \frac{W}{2V_g}$, that is, if the time a MT stays attached to a force generator is sufficiently small compared to the time it takes for a MT to grow across the cell. Thus, the centrosome is driven to oscillate if pulling forces are sufficiently strong and the detachment of MTs from force generators is sufficiently fast.

These calculations and simulations point to an intuitive picture for how oscillations can occur with cortical pulling forces. Since the velocity of a growing MT plus-end is a sum of the MT's polymerization velocity in the direction of growth and the centrosome velocity (Fig. 6e)[46], the motion of a centrosome away from a force generator reduces the rate of MT impingement on that force generator, whereas motion towards a force generator increases the rate of impingement. This results in a decreased probability of attachment and, hence, a decreased force from force generators behind the centrosome. It also results in an increased probability of attachment and, thus, an increased force in front of the centrosome. This self-reinforcing process move the centrosome over the midpoint ($Y = 0$). However, a forward-moving centrosome eventually reduces in speed due to a geometric effect. When the centrosome is closer to a surface, the force generators pulling it onwards do so from increasingly oblique angles, decreasing their pulling efficacy (Fig. 6f). Once the centrosome speed has slowed down, the MT impingement rate behind the centrosome gradually recovers, eventually stopping the centrosome. Then, MTs reattach to the force generators on the distal side of the centrosome, leading to a larger restoring force (because of the geometric effect) and, hence, oscillations. This phenomenology is robust to details of the system's geometry. The coarse-grained model also predicts that centrosome oscillations can occur between two flat plates.

One key assumption of the model is that MTs that contact the cortex undergo a catastrophe and depolymerize. Because of this effect, the simulations predict that the density of (transverse) MTs between the centrosome and the cortex oscillates out of phase with the centrosome's transverse position (Fig. 6g), which also occurs experimentally (Fig. 6h and Supplementary Video 7), supporting that MT depolymerization is induced upon contact with the cortex[46].

We next investigated whether the cortical pulling forces are sufficient to explain the stable positioning of the spindle near the cell centre in the prometaphase and metaphase. If the number of cortical force generators is reduced sufficiently in this model, then the centrosome ceases to oscillate and is stably centred (Supplementary Notes), which occurs due to a combination of the geometric effect described above (Fig. 6f) and the stoichiometric interactions between MTs and force generators. That is, each force generator can bind to at most one MT at a time[39]. In the absence of stoichiometric interactions, cortical pulling forces are always destabilizing and can never stably centre centrosomes (Supplementary Notes).

When the centrosome is stably centred, as in the prometaphase and metaphase, the resulting spring constant can be analytically calculated as (Supplementary Notes):

$$k_s \approx \frac{2}{3}\frac{Mf_0}{W}\bar{P}^2$$

Using the same parameters as those that reproduced anaphase spindle oscillations in the stochastic simulations but now lowering only M, the number of cortical force generators, this simulation gives a spring constant for spindle centring of 4.8 pN μm^{-1} (Extended Data Fig. 5b), which is the same order of magnitude as the measurements of Garzon-Coral et al. (16.4 ± 2.1 pN μm^{-1})[16]. Therefore, a model with only cortical pulling forces is sufficient to explain the stable centring of the spindle in the prometaphase and metaphase. A reduction in the number of cortical force generators in the prometaphase and metaphase compared to the anaphase is consistent with the ablation of astral MTs causing more dramatic motions in the anaphase (compare Fig. 1 and Fig. 4) and conclusions from previous studies[14,30,35,37,54–56]. The predicted transition between oscillations and stable positioning upon changing the number of cortical force generators can also account for the observation that gpr-1/2 knockdown prevents oscillations[21].

We next investigated whether cortical pulling forces are sufficient to explain the PNC centration process. We used the same cortical pulling model that reproduced the anaphase oscillations and stable centring in the prometaphase and metaphase and assumed that there was the same number of cortical force generators as in the prometaphase and metaphase. The coarse-grained theory can be used to analytically calculate (Supplementary Notes) that the PNC should exponentially approach the centre with a timescale τ_c given by:

$$\frac{1}{\tau_c} = \frac{1}{2}\left(\bar{\Omega} + \kappa\right)\left(1 - \frac{M}{M_c}\right)$$

Fig. 6 | Coarse-grained model of cortical pulling and model predictions. **a**, Key processes in the coarse-grained model. From left to right, MTs grow from their plus-ends with velocity V_g and undergo a catastrophe (that is, a switch from growing to shrinking) with rate λ. MTs that hit the cell cortex without binding to a force generator undergo an immediate catastrophe. MTs that hit an unoccupied force generator bind to it and experience a pulling force f_0. Bound MTs detach from force generators at a rate κ, whereupon they undergo a catastrophe. **b**, Geometry of the coarse-grained model. The cell is treated as a sphere of radius W decorated with force generators (FG, yellow discs). The centrosome (green sphere) is located at a distance Y (along the y axis) from the centre of the cell. $\hat{\boldsymbol{\xi}}$ is a unit vector extending from the centrosome to an FG. Ω is the impingement rate of MTs onto a FG. **c**, To illustrate the mechanism of oscillations, it is helpful to investigate the forces exerted on the centrosome from small regions (polar caps) above and below the centrosomes (upper schematic). The plots show the simulated oscillation amplitude and the net cortical forces from FGs in these polar cap regions. Note that in the simulations, all astral MTs bound to force generators exert forces on the centrosomes (that is, not just those in the polar cap regions). **d**, From a simulation of oscillations with the coarse-grained model, the probability of a cortical force generator being bound is $P(\varphi, t)$, which is a function of polar angle φ from the y axis and time, as displayed by the colour scale in the bottom colour bar. This information is expressed for a cross section through the sphere containing the y axis. The black arrows drawn on centrosomes indicate their velocities. The green field shows the centrosomal MT directions and the front of unattached plus-ends. **e**, Relations among the centrosome speed V_c, the MT growth (polymerization) speed V_g and the speeds of MT plus-ends $V_{MT(+)}$. **f**, Schematic of the geometric effects that lead to the restoring mechanism during oscillations. Viewed from the embryo posterior end, the centrosome oscillates along the y direction on the y–z plane (right panel). As the centrosome approaches the upper surface, the forces from FGs above the centrosome become more oblique, leading to a smaller upward force projected along the y axis. **g**–**i**, Theoretical predictions and experimental measurements of astral MT density and pronuclear centration. **g**, The simulation predicted that the density of astral MTs (lower, yellow curve) within an annular sector along the transverse direction oscillates out of phase with the transverse position of the centrosome (upper, blue curve). **h**, Experimental measurement of the centrosomes' transverse amplitudes and the intensities of astral MTs within annular sectors (60°, 3 μm inner radius, 9 μm outer radius, as the yellow frame on the image) of the transverse directions. Altogether, 44 oscillation cycles were extracted from 11 embryos (Methods). Scale bar, 10 μm. **i**, The simulated (upper) and experimental (lower, $n = 10$) results of pronuclear centration with exponential fits (dark red curves) and the resulting centring timescales $\tau_{c,sim}$ and $\tau_{c,exp}$. The distance is calculated from the centrosome to the sphere centre in simulations, and experimentally from the PNC centre to the embryo centre along the longitudinal direction. Experimental data in **h** and **i** are presented with mean value curves and SEM error bars overlaying the semitransparent raw data curves.

https://doi.org/10.1038/s41567-023-02223-z

Consistent with this prediction, exponential relaxation was observed in both simulations and experiments (Fig. 6i and Extended Data Fig. 5a), with timescales of 26 and 32 s, respectively (95% confidence interval, 29–36 s in our experiments). A second prediction of the coarse-grained theory is that the centring timescale τ_c is the same as the timescale τ_f of approach to a new equilibrium in response to an applied force. Consistent with this prediction, the observed centring times quoted above are the same as the force response timescale found

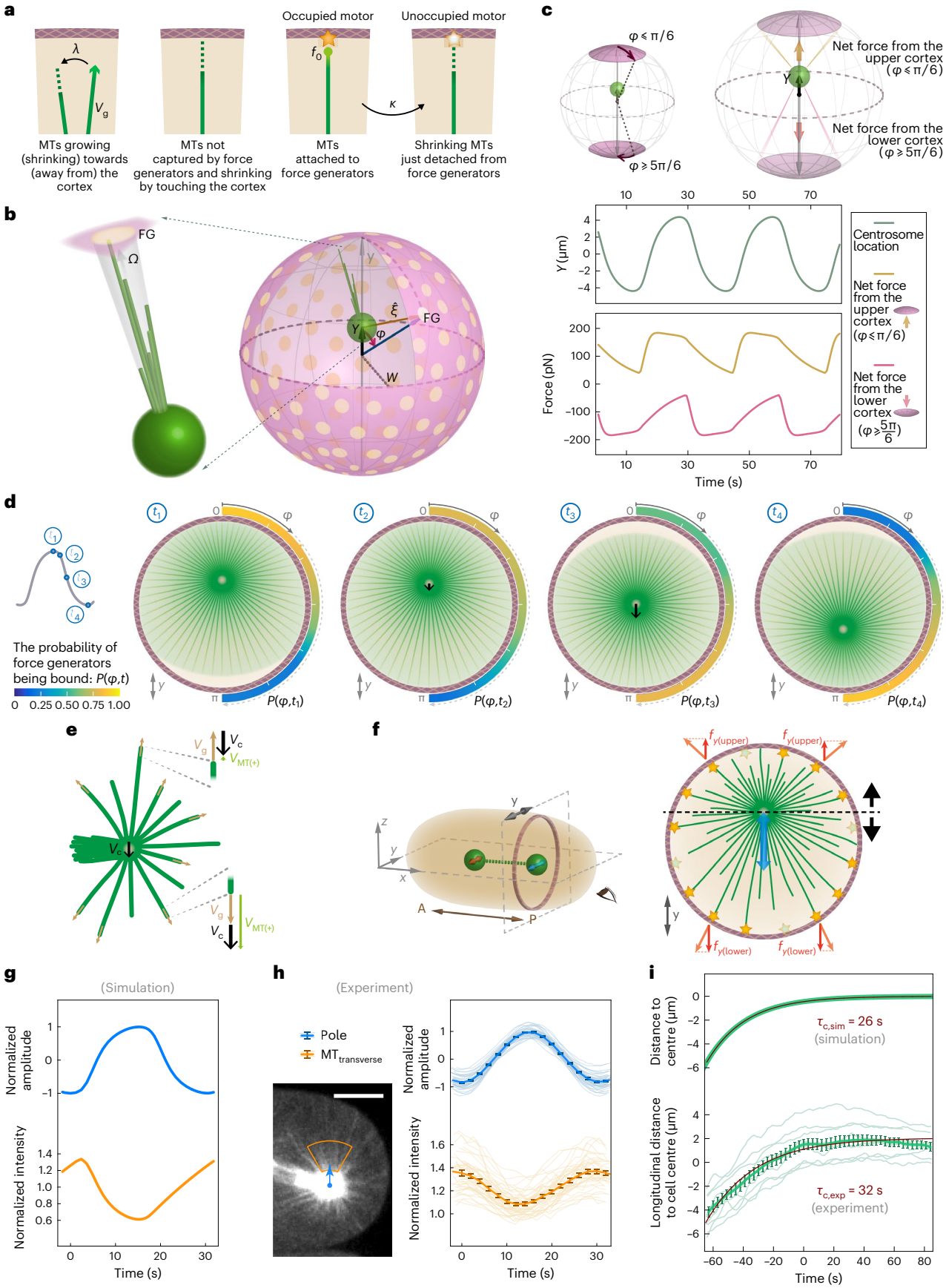

in simulations of the coarse-grain model, $\tau_{f,sim} = 25$ s, and previously experimentally measured $\tau_{f,exp} = 28$ s (95% confidence interval, 26–31 s, from Supplementary Fig. 13 in Garzon-Coral et al.[16]).

Conclusion

We have shown that cortical pulling forces drive pronuclear migration and rotation as well as spindle centring, elongation and oscillations in *C. elegans* embryos, with no discernible contribution from MT pushing or cytoplasmic pulling forces. This was accomplished using a combination of FESLA (to distinguish between pushing and pulling), fluid flow analysis (to differentiate between cytoplasmic and cortical pulling) and coarse-grained modelling. Previous work demonstrated that the asymmetric positioning of the spindle can also be explained by cortical pulling forces[39]. Thus, cortical pulling forces are sufficient to drive the diverse cell biological behaviour of centrosomes including directed motions, stable positioning and oscillations. Since such centrosome behaviours are observed in diverse contexts[7,12–20], as are cortical pulling forces[38], the principles we have uncovered here should be broadly applicable to other systems.

Online content

Any methods, additional references, Nature Portfolio reporting summaries, source data, extended data, supplementary information, acknowledgements, peer review information; details of author contributions and competing interests; and statements of data and code availability are available at https://doi.org/10.1038/s41567-023-02223-z.

References

1. Knoblich, J. A. Asymmetric cell division: recent developments and their implications for tumour biology. *Nat. Rev. Mol. Cell Biol.* **11**, 849–860 (2010).
2. Kotak, S., Busso, C. & Gönczy, P. Cortical dynein is critical for proper spindle positioning in human cells. *J. Cell Biol.***199**, 97–110 (2012).
3. Siller, K. H. & Doe, C. Q. Spindle orientation during asymmetric cell division. *Nat. Cell Biol.* **11**, 365–374 (2009).
4. Kiyomitsu, T. & Cheeseman, I. M. Chromosome- and spindle-pole-derived signals generate an intrinsic code for spindle position and orientation. *Nat. Cell Biol.* **14**, 311–317 (2012).
5. Pearson, C. G. & Bloom, K. Dynamic microtubules lead the way for spindle positioning. *Nat. Rev. Mol. Cell Biol.* **5**, 481–492 (2004).
6. Tame, M. A. et al. Astral microtubules control redistribution of dynein at the cell cortex to facilitate spindle positioning. *Cell Cycle* **13**, 1162–1170 (2014).
7. von Dassow, G., Verbrugghe, K. J., Miller, A. L., Sider, J. R. & Bement, W. M. Action at a distance during cytokinesis. *J. Cell Biol.* **187**, 831–845 (2009).
8. Minc, N., Burgess, D. & Chang, F. Influence of cell geometry on division-plane positioning. *Cell* **144**, 414–426 (2011).
9. Reinsch, S. & Gonczy, P. Mechanisms of nuclear positioning—Commentary. *J. Cell Sci.* **111**, 2283–2295 (1998).
10. Reinsch, S. & Karsenti, E. Movement of nuclei along microtubules in *Xenopus* egg extracts. *Curr. Biol.* **7**, 211–214 (1997).
11. Rujano, M. A., Sanchez-Pulido, L., Pennetier, C., le Dez, G. & Basto, R. The microcephaly protein Asp regulates neuroepithelium morphogenesis by controlling the spatial distribution of myosin II. *Nat. Cell Biol.* **15**, 1294–1306 (2013).
12. Longo, F. J. & Anderson, E. The fine structure of pronuclear development and fusion in the sea urchin, *Arbacia punctulata*. *J. Cell Biol.* **39**, 339–368 (1968).
13. Meaders, J. L. & Burgess, D. R. Microtubule-based mechanisms of pronuclear positioning. *Cells* **9**, 505 (2020).
14. Cowan, C. R. & Hyman, A. A. Asymmetric cell division in *C. elegans*: cortical polarity and spindle positioning. *Annu. Rev. Cell Dev. Biol.* **20**, 427–453 (2004).
15. Tanimoto, H., Sallé, J., Dodin, L. & Minc, N. Physical forces determining the persistency and centring precision of microtubule asters. *Nat. Phys.* **14**, 848–854 (2018).
16. Garzon-Coral, C., Fantana, H. A. & Howard, J. A force-generating machinery maintains the spindle at the cell center during mitosis. *Science* **352**, 1124–1127 (2016).
17. Foe, V. E. & von Dassow, G. Stable and dynamic microtubules coordinately shape the myosin activation zone during cytokinetic furrow formation. *J. Cell Biol.* **183**, 457–470 (2008).
18. Du, Q. & Macara, I. G. Mammalian Pins is a conformational switch that links NuMA to heterotrimeric G proteins. *Cell* **119**, 503–516 (2004).
19. Riche, S. et al. Evolutionary comparisons reveal a positional switch for spindle pole oscillations in *Caenorhabditis* embryos. *J. Cell Biol.* **201**, 653–662 (2013).
20. Zhu, M. et al. MISP is a novel Plk1 substrate required for proper spindle orientation and mitotic progression. *J. Cell Biol.* **200**, 773–787 (2013).
21. Pecreaux, J. et al. Spindle oscillations during asymmetric cell division require a threshold number of active cortical force generators. *Curr. Biol.* **16**, 2111–2122 (2006).
22. Grill, S. W., Kruse, K. & Jülicher, F. Theory of mitotic spindle oscillations. *Phys. Rev. Lett.* **94**, 108104 (2005).
23. Grill, S. W., Gonczy, P., Stelzer, E. H. & Hyman, A. A. Polarity controls forces governing asymmetric spindle positioning in the *Caenorhabditis elegans* embryo. *Nature* **409**, 630–633 (2001).
24. Grill, S. W., Howard, J., Schaffer, E., Stelzer, E. H. & Hyman, A. A. The distribution of active force generators controls mitotic spindle position. *Science* **301**, 518–521 (2003).
25. Bellanger, J. M. et al. ZYG-9, TAC-1 and ZYG-8 together ensure correct microtubule function throughout the cell cycle of *C. elegans* embryos. *J. Cell Sci.* **12016**, 2963–2973 (2007).
26. Hyman, A. A. & White, J. G. Determination of cell division axes in the early embryogenesis of *Caenorhabditis elegans*. *J. Cell Biol.* **105**, 2123–2135 (1987).
27. Le Bot, N., Tsai, M. C., Andrews, R. K. & Ahringer, J. TAC-1, a regulator of microtubule length in the *C. elegans* embryo. *Curr. Biol.* **13**, 1499–1505 (2003).
28. Srayko, M., Quintin, S., Schwager, A. & Hyman, A. A. *Caenorhabditis elegans* TAC-1 and ZYG-9 form a complex that is essential for long astral and spindle microtubules. *Curr. Biol.* **13**, 1506–1511 (2003).
29. Wright, A. J. & Hunter, C. P. Mutations in a β-tubulin disrupt spindle orientation and microtubule dynamics in the early *Caenorhabditis elegans* embryo. *Mol. Biol. Cell* **14**, 4512–4525 (2003).
30. Colombo, K. et al. Translation of polarity cues into asymmetric spindle positioning in *Caenorhabditis elegans* embryos. *Science* **300**, 1957–1961 (2003).
31. Bringmann, H., Cowan, C. R., Kong, J. & Hyman, A. A. LET-99, GOA-1/GPA-16, and GPR-1/2 are required for aster-positioned cytokinesis. *Curr. Biol.* **17**, 185–191 (2007).
32. Goulding, M. B., Canman, J. C., Senning, E. N., Marcus, A. H. & Bowerman, B. Control of nuclear centration in the *C. elegans* zygote by receptor-independent Gα signaling and myosin II. *J. Cell Biol.* **178**, 1177–1191 (2007).
33. Galli, M. et al. aPKC phosphorylates NuMA-related LIN-5 to position the mitotic spindle during asymmetric division. *Nat. Cell Biol.* **13**, 1132–1138 (2011).
34. Tsou, M. F., Hayashi, A., DeBella, L. R., McGrath, G. & Rose, L. S. LET-99 determines spindle position and is asymmetrically enriched in response to PAR polarity cues in *C. elegans* embryos. *Development* **129**, 4469–4481 (2002).
35. Nguyen-Ngoc, T., Afshar, K. & Gonczy, P. Coupling of cortical dynein and Gα proteins mediates spindle positioning in *Caenorhabditis elegans*. *Nat. Cell Biol.* **9**, 1294–1302 (2007).

36. Krueger, L. E., Wu, J. C., Tsou, M. F. & Rose, L. S. LET-99 inhibits lateral posterior pulling forces during asymmetric spindle elongation in *C. elegans* embryos. *J. Cell Biol.* **189**, 481–495 (2010).
37. Gotta, M., Dong, Y., Peterson, Y. K., Lanier, S. M. & Ahringer, J. Asymmetrically distributed *C. elegans* homologs of AGS3/PINS control spindle position in the early embryo. *Curr. Biol.* **13**, 1029–1037 (2003).
38. Wu, H.-Y., Nazockdast, E., Shelley, M. J. & Needleman, D. J. Forces positioning the mitotic spindle: theories, and now experiments. *BioEssays* **39**, 1600212 (2017).
39. Farhadifar, R. et al. Stoichiometric interactions explain spindle dynamics and scaling across 100 million years of nematode evolution. *eLife* **9**, e55877 (2020).
40. Yu, C.-H. et al. Central-spindle microtubules are strongly coupled to chromosomes during both anaphase A and anaphase B. *Mol. Biol. Cell* **30**, 2503–2514 (2019).
41. Chung, S. H., Clark, D. A., Gabel, C. V., Mazur, E. & Samuel, A. D. The role of the AFD neuron in *C. elegans* thermotaxis analyzed using femtosecond laser ablation. *BMC Neurosci.* **7**, 30 (2006).
42. Chung, S. H. & Mazur, E. Surgical applications of femtosecond lasers. *J. Biophotonics* **2**, 557–572 (2009).
43. Gabel, C. V., Antoine, F., Chuang, C.-F., Samuel, A. D. & Chang, C. Distinct cellular and molecular mechanisms mediate initial axon development and adult-stage axon regeneration in *C. elegans*. *Development* **135**, 1129–1136 (2008).
44. Gabel, C. V. et al. Neural circuits mediate electrosensory behavior in *Caenorhabditis elegans*. *J. Neurosci.* **27**, 7586–7596 (2007).
45. Vogel, A., Noack, J., Hüttman, G. & Paltauf, G. Mechanisms of femtosecond laser nanosurgery of cells and tissues. *Appl. Phys. B* **81**, 1015–1047 (2005).
46. Kozlowski, C., Srayko, M. & Nedelec, F. Cortical microtubule contacts position the spindle in *C. elegans* embryos. *Cell* **129**, 499–510 (2007).
47. Kimura, A. & Onami, S. Computer simulations and image processing reveal length-dependent pulling force as the primary mechanism for *C. elegans* male pronuclear migration. *Dev. Cell* **8**, 765–775 (2005).
48. Kimura, K. & Kimura, A. Intracellular organelles mediate cytoplasmic pulling force for centrosome centration in the *Caenorhabditis elegans* early embryo. *Proc. Natl Acad. Sci. USA* **108**, 137–142 (2011).
49. Shinar, T., Mana, M., Piano, F. & Shelley, M. J. A model of cytoplasmically driven microtubule-based motion in the single-celled *Caenorhabditis elegans* embryo. *Proc. Natl Acad. Sci. USA* **108**, 10508–10513 (2011).
50. Xie, J. & Minc, N. Cytoskeleton force exertion in bulk cytoplasm. *Front. Cell Dev. Biol.* https://doi.org/10.3389/fcell.2020.00069 (2020).
51. Gusnowski, E. M. & Srayko, M. Visualization of dynein-dependent microtubule gliding at the cell cortex: implications for spindle positioning. *J. Cell Biol.* **194**, 377–386 (2011).
52. Laan, L. et al. Cortical dynein controls microtubule dynamics to generate pulling forces that position microtubule asters. *Cell* **148**, 502–514 (2012).
53. Redemann, S. et al. Membrane invaginations reveal cortical sites that pull on mitotic spindles in one-cell *C. elegans* embryos. *PLoS ONE* **5**, e12301 (2010).
54. Schmidt, R. et al. Two populations of cytoplasmic dynein contribute to spindle positioning in *C. elegans* embryos. *J. Cell Biol.* **216**, 2777–2793 (2017).
55. Srinivasan, D. G., Fisk, R. M., Xu, H. & van den Heuvel, S. A complex of LIN-5 and GPR proteins regulates G protein signaling and spindle function in *C. elegans*. *Genes Dev.* **17**, 1225–1239 (2003).
56. Couwenbergs, C. et al. Heterotrimeric G protein signaling functions with dynein to promote spindle positioning in *C. elegans*. *J. Cell Biol.* **179**, 15–22 (2007).
57. Daniels, B. R., Masi, B. C. & Wirtz, D. Probing single-cell micromechanics in vivo: the microrheology of *C. elegans* developing embryos. *Biophys. J.* **90**, 4712–4719 (2006).
58. Valentine, M. T. et al. Colloid surface chemistry critically affects multiple particle tracking measurements of biomaterials. *Biophys. J.* **86**, 4004–4014 (2004).
59. Mochalin, V. N., Shenderova, O., Ho, D. & Gogotsi, Y. The properties and applications of nanodiamonds. *Nat. Nanotechnol.* **7**, 11–23 (2012).
60. Fu, C.-C. et al. Characterization and application of single fluorescent nanodiamonds as cellular biomarkers. *Proc. Natl Acad. Sci. USA* **104**, 727–732 (2007).
61. Mohan, N., Chen, C.-S., Hsieh, H.-H., Wu, Y.-C. & Chang, H.-C. In vivo imaging and toxicity assessments of fluorescent nanodiamonds in *Caenorhabditis elegans*. *Nano Lett.* **10**, 3692–3699 (2010).
62. Vaijayanthimala, V. et al. The long-term stability and biocompatibility of fluorescent nanodiamond as an in vivo contrast agent. *Biomaterials* **33**, 7794–7802 (2012).
63. Chang, Y.-R. et al. Mass production and dynamic imaging of fluorescent nanodiamonds. *Nat. Nanotechnol.* **3**, 284–288 (2008).
64. Su, L.-J. et al. Fluorescent nanodiamonds enable quantitative tracking of human mesenchymal stem cells in miniature pigs. *Sci. Rep.* **7**, 45607 (2017).
65. Howard, J. Mechanics of motor proteins and the cytoskeleton. *Appl. Mech. Rev.* **55**, B39 (2002).
66. Coffman, V. C., McDermott, M. B., Shtylla, B. & Dawes, A. T. Stronger net posterior cortical forces and asymmetric microtubule arrays produce simultaneous centration and rotation of the pronuclear complex in the early *Caenorhabditis elegans* embryo. *Mol. Biol. Cell* **27**, 3550–3562 (2016).
67. Grill, S. W. & Hyman, A. A. Spindle positioning by cortical pulling forces. *Dev. Cell* **8**, 461–465 (2005).

Methods

Experimental subjects

Worm strains. The *C. elegans* line *AZ244 (unc-119(ed3) III; ruIs57[unc-119(+) pie-1::GFP::tubulin])* and a new line *DJN004 (unc-119(ed3) III; ruIs57[unc-119(+) pie-1::GFP::tubulin; [mCherry::tbg-1])* obtained by crossing *AZ244* with a line expressing mCherry-labelled γ-tubulin were used throughout this study. Additionally, to visualize chromosomes, *SA250 (tjIs54 [pie-1p::GFP::tbb-2 + pie-1p::2xmCherry::tbg-1 + unc-119(+)]; tjIs57 [pie-1p::mCherry::his-48 + unc-119(+)])* were used for the metaphase experiments shown in Fig. 4a–d. This line helped to determine the timing of the metaphase and ensure that the chromosomes were not ablated.

***C. elegans* culturing conditions and embryo preparation.** Worms were grown on nematode growth medium plates seeded with OP50 *Escherichia coli* bacteria and incubated at 24 °C. Gravid *C. elegans* hermaphrodites were dissected by needle tips to release their embryos into M9 buffer. Then, mouth pipettes were used to pick and transfer early embryos onto flat 4% agarose pads (Bio-Rad), which were prepared on microscopic slides[68]. A freshly made agarose pad was promptly trimmed to a size smaller than the area of a coverslip. After adding a small amount of M9 buffer to keep the embryos moist, the sample was covered with a coverslip and sealed swiftly for imaging. Under this mounting condition, embryos were slightly squeezed and were held in place by the sunk agarose pad.

After the embryos were prepared, they were imaged either at 22 °C or 18 °C. For different laser-ablation conditions, each set of embryos, including both control uncut and ablated embryos, were imaged at the same temperature for comparison (either all at 22 °C or all at 18 °C).

Experimental methods

Microscopy and imaging. We imaged mounted early *C. elegans* embryos on an inverted microscope (Nikon, TE2000) using a ×60 water-immersion objective (Nikon, CFI Plan Apo VC 60X WI, NA 1.2). Images were acquired using a spinning-disc confocal unit (Yokugawa, CSU-X1) equipped with continuous-wave lasers for fluorescence excitation and an electron-multiplying charge-coupled device (Hamamatsu, ImagEM Enhanced C9100-13) for detection. GFP fluorescence was excited at 488 nm and collected through a bandpass filter with 514 nm centre and 30 nm full width at half maximum (FWHM) wavelength. mCherry fluorescence was excited at 561 nm and collected through a bandpass filter with 593 nm centre and 40 nm FWHM wavelength. The FNDs were excited at 561 nm and collected through a long-pass filter with a 647 nm cut-on wavelength.

All images displayed in the figures and videos in this article were processed in MATLAB (MathWorks) or ImageJ.

Extended Data Fig. 1a indicates the terminology for embryo orientation and axis labels used throughout this manuscript. The x–y midplane is defined as the imaging plane. The longitudinal direction (or the long axis) of an oblong embryo is assigned as the x direction, whereas the transverse direction is in the y direction.

Femtosecond stereotactic laser ablation. Our laser-ablation setup was incorporated into an inverted microscope with a spinning-disc unit (Fig. 1c). A near-infrared Ti:sapphire femtosecond pulsed laser beam with a reduced repetition rate (16–80 kHz, compared to the common 80 MHz repetition rate output)[41–45] was directed and merged into the microscope light path through a dichroic mirror. The ablation laser pulses were focused onto the sample by the same high-numerical-aperture objective used for confocal imaging. We used two different methods to reduce the repetition rate of the femtosecond laser pulses: (1) Using a cavity-dumped Ti:sapphire laser (Cascade-1, KML, with 830–840 nm centre wavelength and 20–30 fs pulse width) with either a 40 kHz pulse train with 2.5–4 nJ pulse energy (the energy measured under our ×60 water-immersion objective) or an 80 kHz pulse train with 2.5–3.5 nJ pulse energy. (2) Using a pulse picker (Eclipse, KMLabs) to select a 16 kHz pulse train from the 80 MHz Ti:sapphire laser pulses (Mai-Tai, Spectra-Physics, with 800 nm centre wavelength and ~70 fs pulse width).

We ablated complex patterns by moving the sample on a three-axis piezo-stage (P-545 PInano XYZ, Physik Instrumente) and controlling laser exposure with a fast mechanical shutter (Newport). Ablation patterns and image acquisition were controlled with custom LabVIEW codes. The dimensions of the FESLA ablated regions are displayed in extended data figures: (1) For experiments during the late metaphase to anaphase spindle oscillations, see Extended Data Fig. 2a (for arc cuts in Fig. 1e–j), Extended Data Fig. 2e (for double rectangular plane cuts), Extended Data Fig. 2f (for open-cylindrical cuts in Fig. 2a–e) and Extended Data Fig. 2i (for cup cuts in Fig. 2f–i). (2) For experiments during the metaphase, see Extended Data Fig. 4a,b (for rectangular plane cuts in Fig. 4a,b) and Extended Data Fig. 4c,d (for cup cuts in Fig. 4c,d). (3) For experiments during the PNC stage, see Extended Data Fig. 4e (for rectangular plane cuts in Fig. 5a,b) and Extended Data Fig. 4h (for large semicircular arc cuts in Fig. 5f–h).

Fluorescent nanodiamonds. Passivated FNDs were used as tracer particles to visualize cytoplasmic flows. We adopted a two-step surface treatment to coat FNDs with mono-methyl polyethylene glycol (mPEG). FNDs (40–50 nm in diameter, after acid wash treatment, a gift from Dr Huan-Cheng Chang)[60–62,64] in Milli-Q water were sonicated for 30 min and then mixed with α-lactalbumin (Sigma, α-lactalbumin from calcium-depleted bovine milk) at a weight ratio of FND:α-lactalbumin of 1:2. The mixture was gently shaken overnight at 4 °C, and then washed through a centrifugal filter (Amicon Ultra, 100 kDa) several times. The FND concentrate was dispersed in Milli-Q water again and sonicated in ice water bath for 15 min and then optionally syringe filtered (Millex-VV, 0.1 µm, Durapore polyvinylidene fluoride membrane). After diluting the solution of FND (with absorbed α-lactalbumin) to ~0.1 mg ml^{-1}, boric acid was added to reach a final concentration of 5 mM and the pH was adjusted to 8. For the second mPEG coating, fresh mPEG-SVA (mPEG-succinimidyl valerate, mol. wt. 5,000, Laysan Bio) was added to a weight ratio of FND: mPEG-SVA ≈ 1:1, and the mixture was stirred overnight at 4 °C. Then, the FNDs were washed through a centrifugal filter several times and dispersed in Milli-Q water. Immediately before use, the FND solution was sonicated in an ice water bath for 15 min, syringe filtered (Pall Acrodisc, 0.2 µm, HT Tuffryn membrane) and diluted to a concentration of 0.25–1 mg ml^{-1}.

We microinjected freshly coated FNDs (within 48 h) into the distal gonads of *AZ244* (unc-119(ed3) III; ruIs57[unc-119(+) pie-1::GFP::tubulin]) young adult hermaphrodites using needles pulled from borosilicate glass capillaries (World Precision Instruments,1.0 mm outer diameter, 0.58 mm internal diameter, with filament) with a P-87 micropipette puller (Sutter Instrument). We cut the hermaphrodites 6–10 h after microinjection and retrieved their embryos for imaging.

We imaged *AZ244* embryos with injected FNDs at 18 °C. Time-lapse z-stack confocal images of both GFP::β-tubulin and FND were acquired every 2.5–5 s. Centrosomes were visualized in GFP::β-tubulin images, which included several z sections with 1 µm spacing and were taken around PNCs or spindles. FND signals were captured through z stacks having 9 or 15 z section images with 1 µm spacing.

Quantification and data analysis

All image analyses and data quantification for experimental data were done in MATLAB (MathWorks). Numerical simulations and their analyses were also done in MATLAB.

Tracking centrosomes. The locations of centrosomes were extracted from either fluorescent γ-tubulin or fluorescent β-tubulin (Extended Data Fig. 1b). For γ-tubulin images (Extended Data Fig. 1b, upper right), we adopted the particle-finding codes from the MATLAB Particle

Tracking Code Repository by D. Blair and E. Dufresne (http://site.physics.georgetown.edu/matlab/) (adapted from IDL Particle Tracking software from David D. Grier, John C. Crocker and Eric R. Weeks)[69] to find the centrosome locations. We used high-pass background subtraction followed by thresholding and identification of local maxima. Subpixel localization of the anterior and posterior centrosomes (orange and blue circles on the upper right image of Extended Data Fig. 1b) was achieved by calculating the centroid near the identified local maximum. For β-tubulin images, the tracking algorithm described above worked well at the PNC stage, but the complex appearance of spindle centrosomes (Extended Data Fig. 1b, lower right image) necessitated an alternative approach. In this case, we used an image-correlation-based approach. We constructed a square region with an artificial ring with a size close to that of a centrosome (Extended Data Fig. 1c, upper), convolved this 'synthetic' centrosome against background-subtracted and thresholded images of spindles (Extended Data Fig. 1c, lower) and identified the position of centrosomes as the local maximum of this correlation (labelled with circles in Extended Data Fig. 1b, lower right image). After acquiring the locations of the centrosomes in each frame (for either γ-tubulin or β-tubulin imaging), we then used the tracking routines from the MATLAB Particle Tracking Code Repository to link these positions into trajectories.

During centrosome oscillations, we defined the longitudinal direction of motion to be along the best-fitting straight line to the combined trajectories of the two centrosomes (Extended Data Fig. 1d). During the metaphase and the PNC stage and for certain ablation data during the oscillations, we instead defined the longitudinal direction of motion by an embryo's geometry. We determined the cell boundary by thresholding (and smoothing) the β-tubulin image (Extended Data Fig. 1e, purple), fitted the contour to an ellipse (Extended Data Fig. 1e, dashed yellow) and used the long axis of the ellipse as the longitudinal direction (Extended Data Fig. 1e, solid yellow line). We defined the location of the anterior and posterior ends of the embryo to be the location on the embryo contour that intersected with this longitudinal axis (Extended Data Fig. 1f). We defined the transverse direction to be orthogonal to the longitudinal direction.

Analysis of spindle oscillations. Centrosome motions. To determine the amplitude and timing of centrosome oscillations, we examined the transverse position of the centrosomes, obtained rough peak positions by identifying local maximum and minima after smoothing the trajectories and then obtained refined peak positions by fitting the raw data for the unsmoothed transverse positions around these local maxima and minima to Gaussians (Extended Data Fig. 1g).

We analysed the impact of laser-ablation arc cuts (Fig. 1e–j and Extended Data Fig. 2a) on oscillations by calculating $\Delta v_y = v_{y(\text{after})} - v_{y(\text{before})}$, the difference in centrosome (y) velocity immediately before $v_{y(\text{before})}$ and after ablation $v_{y(\text{after})}$ (Extended Data Fig. 2b). Ablation itself took a time window τ_w of 2.3 s on average to complete. Velocities were measured by linear fits of transverse centrosome positions over for a mean of 2.7 s (at least three data points, Extended Data Fig. 2c, for example). The resulting change in the centrosome transverse velocity ($\Delta v_y = v_{y(\text{after})} - v_{y(\text{before})}$) was calculated for all arc-cut experiments shown in Fig. 1e,f,h,i (Δv_y in Extended Data Fig. 2d).

We analysed the impact of laser-ablation double rectangular plane cuts (Extended Data Fig. 2e) and open-cylindrical cuts (Fig. 2a–c and Extended Data Fig. 2f) on oscillations by calculating $A_{\text{after}}/A_{\text{before}}$, the ratio of amplitudes for the oscillations immediately before A_{before} and after A_{after} the cuts (Extended Data Fig. 2g). Both double-plane cuts and open-cylindrical cuts exhibited a highly significant difference in the $A_{\text{after}}/A_{\text{before}}$ ratio compared to controls (Extended Data Fig. 2h).

We analysed the impact of laser-ablation cup cuts (Extended Data Fig. 2i) on oscillations by calculating the minimum distance $d_{\min}$ that the centrosome came to the cell boundary after ablation (Extended Data Fig. 2j).

Analysis of astral microtubules. To measure the changes in astral MTs during spindle oscillations, we imaged GFP::β-tubulin in 11 embryos and calculated the intensity of pixels in three annular sectors with a 3 µm inner radius, a 9 µm outer radius and subtended angles of 60° (Extended Data Fig. 6a): an 'up' transverse section oriented in the direction of centrosome motion, a 'down' transverse section oriented in the direction opposite centrosome motion and a 'lateral' section between the centrosome and the lateral cortex. The orientations of the annular sectors remained unchanged while their locations varied as the posterior centrosome moved (Supplementary Video 7). For each embryo, we measured the tubulin intensity with background subtraction in these three regions throughout the five-half-cycle temporal window with the maximal five consecutive peak-to-valley amplitudes (for example, see Extended Data Fig. 6b, left panel). Two full cycles of the upward part (positive y direction, T_1 and T_2) and two full cycles of the downward part (negative y direction, T_3 and T_4) after vertical flipping were taken into consideration (Extended Data Fig. 6b, middle panel), giving a total of 44 full oscillation cycles from 11 embryos. For each full cycle, the time period was rescaled to the mean time period $T_{(\text{m})}$ of the 44 cycles (Extended Data Fig. 6b, right panel), and the intensity values from the transverse region were further normalized by the temporal mean intensity of the lateral region. After aligning the oscillation midpoints at zero, all amplitude values were divided by half the mean transverse displacement (maximum y value minus minimum y value) of the 44 cycles, to set the amplitude nearly between 1 and −1.

To analyse the predicted changes in astral MTs during spindle oscillations from the coarse-grained model, we derived an analytical formula for the total length of MTs in an annular sector (which is analogous to the experimentally measured intensity of tubulin in such a sector). To do this, we consider an angle $\theta' \in [-\pi, \pi]$ encircling the centrosome in the coarse-grained model, where θ' is related to the polar angle φ' (defined in Supplementary Notes Section II.v) by $\theta' = \varphi'$ for $\theta' > 0$ and $\theta' = -\varphi'$ for $\theta' < 0$. Consider a discal sector $S = [D_1, D_2] \times [\theta'_1, \theta'_2]$, where we assume that $D_{1,2} < d(\theta')$ for $\theta'_1 \le \theta' \le \theta'_2$. There are three types of MTs emanating from the centrosome: (1) those with length $l \le D_1$, which contribute nothing to the discal intensity; (2) those with length $D_1 \le l \le D_2$, which contribute a length of $l - D_1$ and (3) those with length $D_2 \le l \le D(\theta')$, which contribute a length of $D_2 - D_1$. Hence, the total MT length in S is

$$L = \int_{\theta'_1}^{\theta'_1} \mathrm{d}\theta' \left[\int_{D_1}^{D_2} \mathrm{d}l\,(l - D_1)\,\psi(l) + \int_{D_2}^{D(\theta')} \mathrm{d}l\,(D_2 - D_1)\,\psi(l) \right]$$
$$= \int_{\theta'_1}^{\theta'_1} \mathrm{d}\theta' \left[1 - \frac{D_2 - D_1}{l_{\text{MT}}} \frac{\exp(-D(\theta')/l_{\text{MT}})}{\exp(-D_1/l_{\text{MT}}) - \exp(-D_2/l_{\text{MT}})} \right]$$

with $l_{\text{MT}} = V_g/\lambda$ and using that $\psi(l) = \frac{\gamma}{V_g} \exp(-l\lambda/V_g)$.

Simulations with the coarse-grained model of cortical pulling. We numerically calculated the centrosome movement using the equations of motion from our coarse-grained model of cortical pulling. Balancing the net force from the force generators (F_{fg}) with the drag force of the centrosome (F_{drag}) gives $F_{\text{drag}} + F_{\text{fg}} = 0$, resulting in

$$\dot{Y} = \frac{Mf_0}{2\eta} \int_0^{\pi} \mathrm{d}\varphi \sin\varphi \frac{W}{\sqrt{W^2 - 2WY\cos\varphi + Y^2}} \left(\cos\varphi - \frac{Y}{W} \right) P(\varphi)$$

And the dynamical equation for P can also be derived from the equations of motion:

$\partial_t P(\varphi) = \Omega(\dot{Y}, Y, \varphi)(1 - P(\varphi)) - \kappa P(\varphi)$, where the impingement rate is given by:

$$\Omega(\dot{Y}, Y, \varphi) = \left(\dot{Y}\cos\varphi + \frac{V_g W - V_g Y \cos\varphi}{d} \right) \frac{1}{2} \left(1 - \frac{1}{\sqrt{1 + (r/d)^2}} \right) \frac{\gamma}{V_g} \mathrm{e}^{-d\lambda/V_g},$$

and $d = \sqrt{W^2 - 2WY\cos\varphi + Y^2}$.

Then, we can numerically calculate the centrosome velocity and position and the probability of force generators being bound using estimated motor numbers for different stages. Using a motor number slightly higher than M_c, we can produce anaphase oscillation behaviours. Using a motor number much lower than M_c while keeping all the other parameters the same, we can simulate PNC centration. Finally, we use the same motor number for PNC to simulate the spindle stable centring in the metaphase as in the experiments of Garzon-Coral et al.[16], where an external force (F_{ext}) was exerted and then released. Under this condition, the force-balance equation becomes:

$$F_{drag} + F_{fg} + F_{ext} = 0$$

We swept the parameters in the simulations to investigate how the biophysical parameters affect the centrosome movements. Extended Data Fig. 5a–c gives examples of pronuclear centration, metaphase stable centring and centrosome oscillation while different parameters were swept. Extended Data Fig. 5d–h demonstrates how varying different parameters affected the outcome observations. Finally, we adopted the parameters shown in Extended Data Table 1, which yielded realistic results like those from the experiments. These simulation data are shown in the main text and figures.

Measuring cytoplasmic fluid flows with FNDs. We measured cytoplasmic fluid flows using FNDs as passive tracer particles. This entailed tracking the motions of individual FNDs and averaging the velocities of FNDs over multiple time points and embryos to determine the fluid flow velocities.

We imaged FNDs in embryos by 3D time-lapse microscopy with either 9 or 15 z sections spaced 1 µm apart. We adopted and modified the MATLAB 3D feature finding algorithms, which were written by Yongxiang Gao and Maria Kilfoil[70] based on IDL codes from John C. Crocker and David G. Grier[69], to extract the FND particle features and obtain their 3D positions with subpixel precision. Then we tracked the 3D trajectory of each individual FND again using the MATLAB Particle Tracking Code Repository. We calculated the 3D instantaneous velocity of every FND, at each time and location, as the difference between its positions at two consecutive frames divided by the time interval between those frames. While tracking FNDs, we also imaged and tracked centrosomes using GFP::β-tubulin images.

To determine the pattern of fluid flow throughout the cytoplasm, we averaged together FND velocities from different time points and embryos. Positioning stages can mainly be recognized through GFP::β-tubulin images. We also used the position and movement of the centrosomes to determine the frames to include and the coordinate system with which to perform this averaging. For spindle oscillations midpoints at time T_m, we selected times in which the posterior centrosome was located within 1 µm transversely from the oscillation midpoint and moving with a transverse speed greater than 0.15 µm s^{-1}. For prometaphase spindles, we included times after rotation had nearly ceased. For metaphase spindles, we included spindles with lengths between 20% and 40% of their embryo lengths and before spindle oscillations had begun. After determining which time points to include, we aligned the position and velocity data based on the locations of the centrosomes and the embryos' anterior-to-posterior directions. Then we projected the 3D positions and instantaneous velocity vectors of the FNDs onto the x–y plane and determined the 2D fluid flow velocity on grid points with 2.5 µm (x) by 2.5 µm (y) spacing (Extended Data Fig. 3a) by averaging FND velocities in overlapping cuboid domains. From the prometaphase to the late anaphase (Figs. 3e and 4g,j), the averaging domain was a 5 µm (x) by 5 µm (y) by 6 µm (z) cuboid with the grid point at the cuboid centre (Extended Data Fig. 3b). To calculate fluid flows around pronuclei (Fig. 5e), we used a 5 µm (x) by 5 µm (y) by 9 µm (z) overlapping averaging domain (Extended Data Fig. 3c). For PNC migration and rotation, we considered two different criteria for averaging: (1) As in the main text (Fig. 5e), we adopted times when the longitudinal distance between the PNC centre and the embryo posterior end measured 35–50% of the embryo length (or R = 0.35–0.5; Extended Data Fig. 3g, left). (2) Alternatively, we used times when the angle A between the PNC axis (centrosome-to-centrosome) and the longitudinal axis of the cell ranged between 33° and 66° (Extended Data Fig. 3d, right). Both methods gave qualitatively similar results.

The averaged experimental velocity vectors were plotted according to a P-value-related colour map. The P value of each cuboid block of 2D velocity data was calculated with a one-sample two-tailed t-test using the lengths of those pooled velocity vectors projected onto the direction of their averaged vector. The null hypothesis is that there is no cytoplasmic flow and particles merely exhibit Brownian motion. The colour map makes those significant flow vectors more prominent to improve visibility. Finally, we drew an imaginary embryo cell contour to represent the averaged cell boundary and removed those data points outside the drawn boundary.

To compare the computational fluid mechanics simulations to the experimental data, we performed analogous projections and averaging. For the simulations, we calculated projected 2D vector fields of fluid flow on 2 µm by 2 µm grids by averaging the continuous velocity field in overlapping domains. For simulations from the prometaphase to the late anaphase (Figs. 3b,c, 4e,f and 4h,i), we used a 4 µm (x) by 4 µm (y) by 6 µm (z) cuboid averaging domain. For simulations at the PNC stage (Fig. 5c,d), we used a 4 µm (x) by 4 µm (y) by 8 µm (z) cuboid averaging domain.

Data availability

All data in this study are available from the corresponding authors upon reasonable request.

Code availability

The codes used in this study are available from the corresponding authors upon reasonable request.

References

68. Walston, T. & Hardin, J. An agar mount for observation of *Caenorhabditis elegans* embryos. *Cold Spring Harb. Protoc.* https://doi.org/10.1101/pdb.prot5540 (2010).
69. Crocker, J. C. & Grier, D. G. Methods of digital video microscopy for colloidal studies. *J. Colloid Interface Sci.* **179**, 298–310 (1996).
70. Gao, Y. & Kilfoi, M. L. Accurate detection and complete tracking of large populations of features in three dimensions. *Opt. Express* **17**, 4685–4704 (2009).

Acknowledgements

Worm strains were provided by M. Delattre and the Caenorhabditis Genetics Center. M.J.S. acknowledges support from the National Science Foundation (NSF) under awards DMR-1420073 (NYU MRSEC) and DMR-2004469. D.J.N. acknowledges NSF grant DBI-1919834, NSF grant 2004380, and the National Institutes of Health grant 1R01GM104976-01. We are grateful to C.-H. Yu who assisted with the optical setup and to C.-Y. Fang for advice on FND surface treatment. We also like to thank R. Farhadifar for helpful discussion over the whole project and advice on modelling, Y.-N. Young for assistance in a technical calculation and J. Howard for helpful discussions.

Author contributions

H.W., D.J.N. and M.J.S. designed the research. H.W. developed the FESLA setup. H.W. conducted all the experiments and data analysis. H.C. provided support for the FND experiments. G.K., E.N. and M.J.S. worked on the large-scale fluid mechanics simulations. M.J.S. and D.J.N. derived and analysed the coarse-grained model. H.W., D.J.N., M.J.S., E.N. and G.K. wrote the paper.

Competing interests
The authors declare no competing interests.

Additional information
Extended data Extended data are available for this paper at https://doi.org/10.1038/s41567-023-02223-z.

Supplementary information The online version contains supplementary material available at https://doi.org/10.1038/s41567-023-02223-z.

Correspondence and requests for materials should be addressed to Hai-Yin Wu.

Peer review information *Nature Physics* thanks Jan Brugues and the other, anonymous, reviewer(s) for their contribution to the peer review of this work.

https://doi.org/10.1038/s41567-023-02223-z

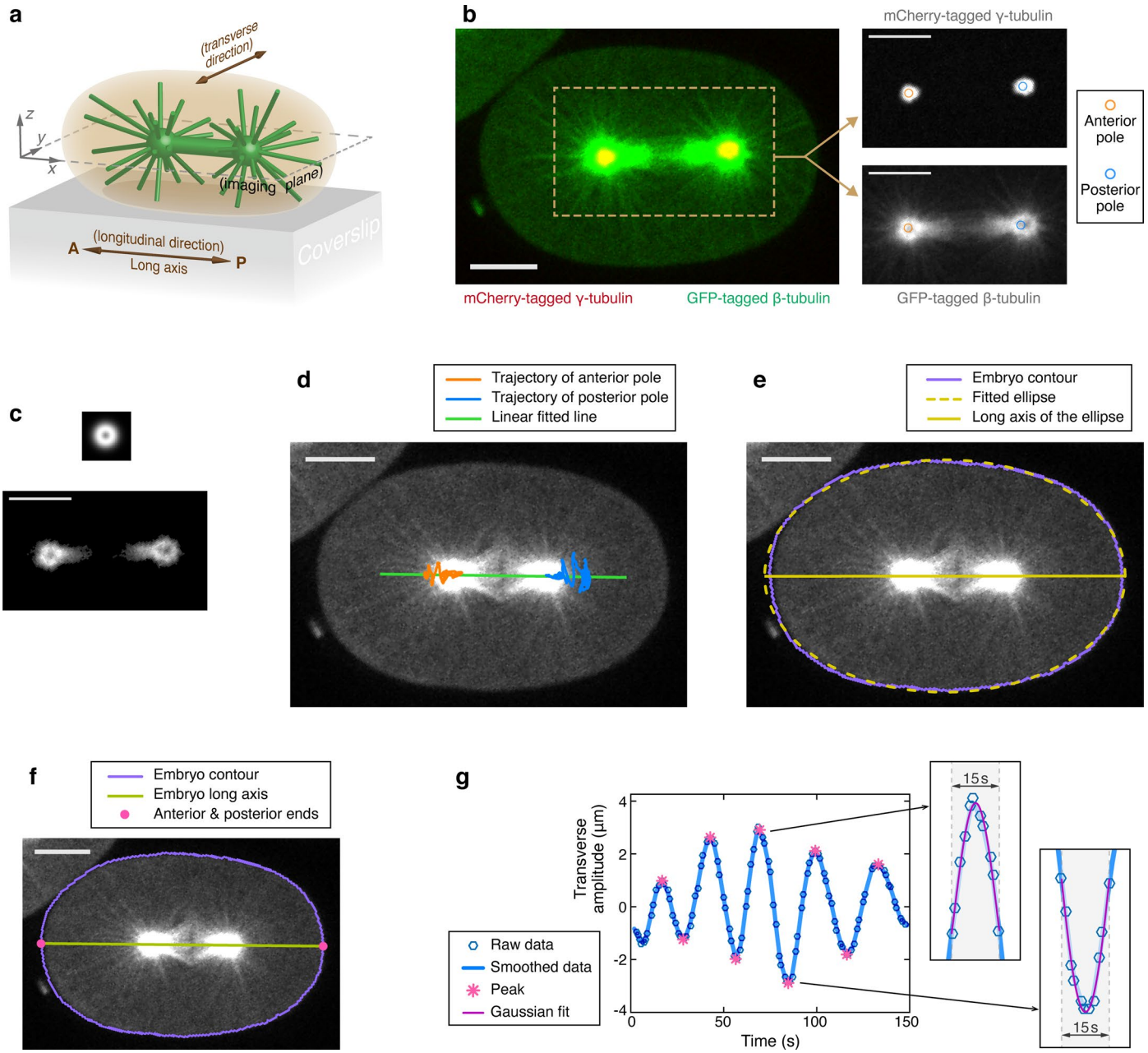

Extended Data Fig. 1 | Orientation terminology, image analysis and centrosome motion quantification. a, The configuration and the terminology of embryo orientation used in this study. The mitotic spindle is simply illustrated by the green dumbbell, while astral MTs illustrated by slender green sticks. The confocal imaging plane, which is parallel to the coverslip, is defined as the *x*-*y* plane, with the $z = 0$ plane falling at the centre of the spindle or the PNC. The embryo's A–P direction is assigned as the longitudinal direction (*x* axis), with the embryo's posterior end facing the positive *x* direction. And the transverse direction refers to the *y* direction. **b**,**c**, An example of the centrosome-tracking image. **b**, The two-colour merged image of an *C. elegans* embryo expressing mCherry-tagged γ-tubulin (red) and GFP-tagged β-tubulin (green). The two separate images of the dashed-line region are shown in the right panel. The upper one is a γ-tubulin-labeling image with its labeled centrosome locations derived by MATLAB Particle Tracking Code Repository by Daniel Blair and Eric Dufresne. The lower one is a β-tubulin-labeling image, while its centrosome information is derived from the particle tracking code plus the second-step correlation method. **c**, Top, the square image patch with the artificial ring structure mimicking a centrosome. Bottom, an example of the post-processed (background-subtraction and thresholding) β-tubulin-labeling image used for correlation calculation. (The top and bottom images are displayed on the same scale.) **d**,**e**, The information of the embryo long axis (or longitudinal direction) can be extracted automatically in two ways: **d**, through linear fitting on the trajectory data of the anterior and posterior centrosomes, or **e**, through fitting the automatic detected embryo contour with a simple ellipse. **f**, An example of the automatic detected embryo contour and the embryo anterior/posterior ends. **g**, An example of oscillation peak detection. The crests/troughs (or the peak points) of the transverse oscillations were calculated by (1) first finding the local maxima/minima from the smoothed amplitude data, and then (2) fitting the raw amplitude data, which fall within the 15-second windows around the above detected maxima/minima, by Gaussian function (see the enlargements). The derived peak points are marked by pink asterisks. All scale bars on images are 10 μm.

https://doi.org/10.1038/s41567-023-02223-z

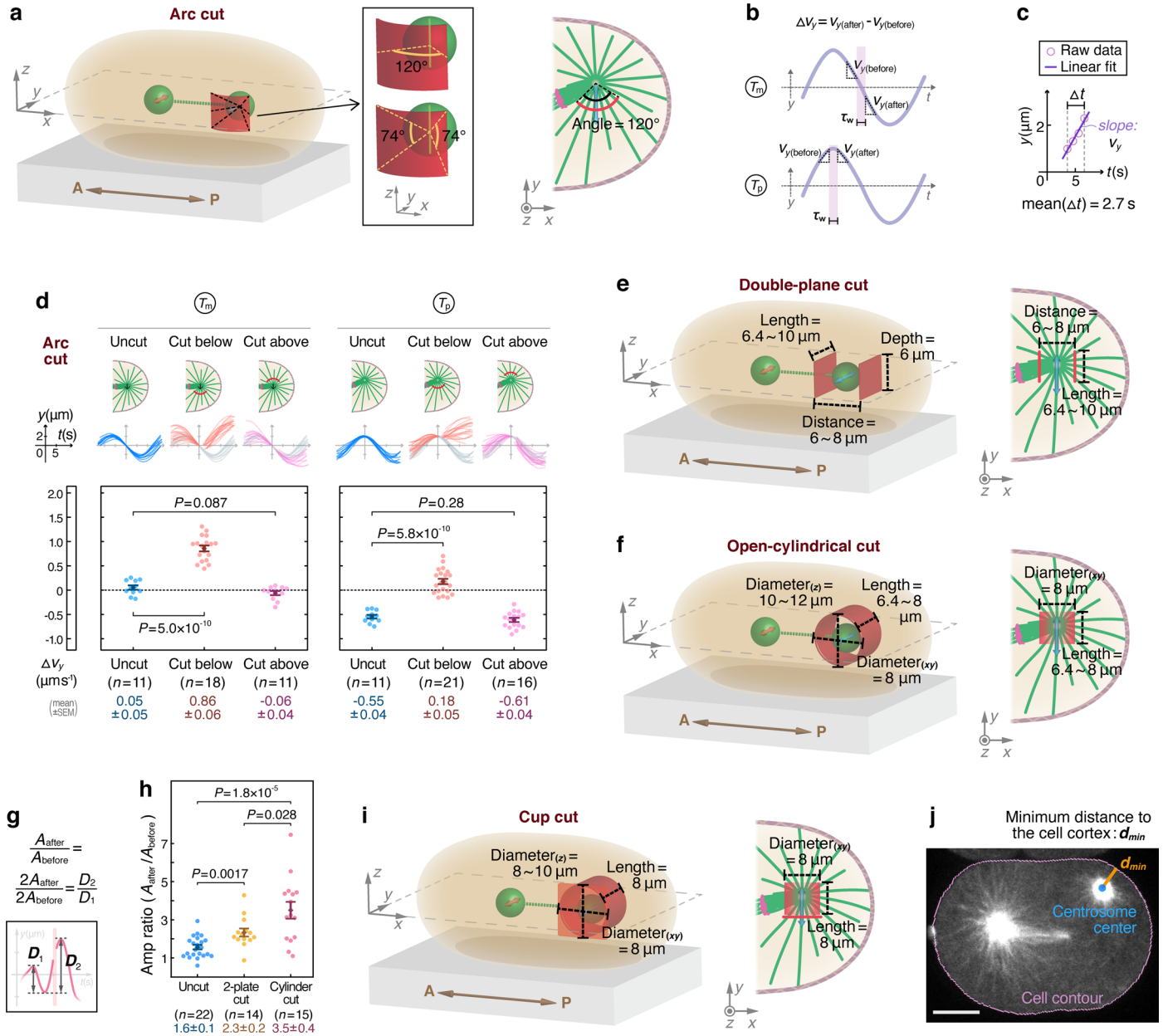

Extended Data Fig. 2 | Dimensions of laser ablations performed during transverse spindle oscillations and the results quantifications. In 3D schematics **a**, **e**, **f**, and **i**, centrosomes are represented by two green balls and the spindle body is simplified into the green dashed line. The A–P direction (embryo polarity) is indicated by the brown arrow. The orange and blue arrows displayed on the centrosomes imply the transverse oscillations of the anterior and posterior centrosomes respectively. The posterior part of the corresponding *x*-*y* imaging midplane (2D view from the top) is exhibited on the right of each 3D schematic, with the spindle and astral MTs sketched in green and chromosomes in magenta. All ablation geometrics are portrayed in red for both 2D and 3D schematics. **a**, Dimensions of the arc cuts in Fig. 1e,f, and h,i (all performed with the same angular span stated here). **b**,**c**, Calculation of centrosome velocity change (Δv_y) for arc cuts. **b**, Definition of Δv_y at timing T_m and T_p respectively. And τ_w is the sandwiched window (for ablated embryos: this window is the ablation execution time) between the two intervals Δt used for calculating centrosome transverse velocity $v_{y(before)}$ and $v_{y(after)}$. **c**, The raw data of centrosome position falling within the interval Δt are used to calculate transverse (y) velocity by linear fitting. **d**, The Δv_y data for uncut (control) and arc-cut embryos. Left, the data for Fig. 1e,f (T_m). Right, the data for Fig. 1h,i (T_p). **e**, A schematic of the double rectangular (*y*-*z*) plane cut and the detailed dimensions. **f**, Dimensions of the open-cylindrical cuts in Fig. 2a–e. **g**, Measurement on oscillation amplitude change by calculating the amplitude ratio A_{after}/A_{before} (mentioned in Fig. 2e). The notation A means oscillation transverse amplitude, and D stands for peak-to-valley transverse amplitude/displacement. The oscillation example (pink curve) is the one from Fig. 2d (open-cylindrical cut). The ablation execution is highlighted by the light pink vertical strip. **h**, The comparison of the amplitude ratios among uncut, double-plane-cut, and open-cylindrical-cut embryos. We found that the more perpendicular MTs that were ablated, the more the oscillation amplitude increased. This is consistent with the perpendicular MTs being subject to pulling forces, and hence constraining centrosome motion. **i**, Dimensions of the cup cuts in Fig. 2f–i. **j**, An example image of calculating the minimum distance to the cell cortex (mentioned in Fig. 2i). The minimum distance, from the posterior centrosome to the cell cortex, of each embryo, is extracted from the time frame with minimal d_{min} (scale bar, 10 μm). All *P* values were calculated by two-tailed Student's *t*-tests (error bars, SEM).

https://doi.org/10.1038/s41567-023-02223-z

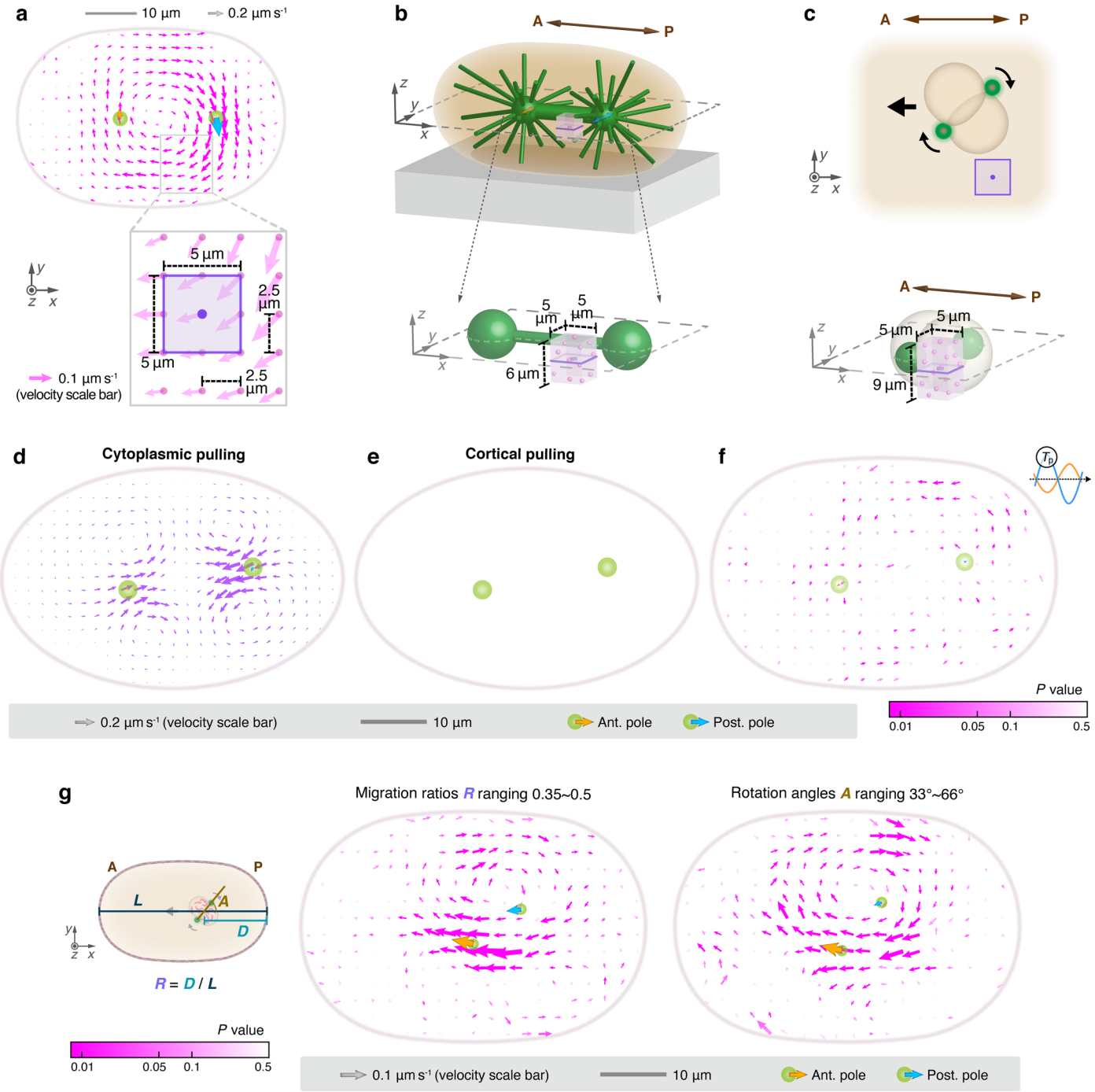

Extended Data Fig. 3 | Averaging operations for experimental flow measurements and fluid results. a, The fluid flow vector field is displayed by 2D vectors (magenta arrows) plotted on grid points with 2.5 μm x spacing and 2.5 μm y spacing (the bottom enlargement). After proper alignment and data grouping, each velocity vector represents the mean *x*-*y* velocity of the FNDs located within the averaging domain surrounding the centre grid point (the purple square frame surrounding the purple dot, further described in **b** and **c**). **b**,**c**, Schematics of the averaging cuboid domain (purple transparent cuboid) with the grid point located at the centre of the cuboid. Centrosomes are illustrated by green balls, and the magenta particles inside the cuboids represent tracked FNDs. The A–P direction is indicated by the brown arrow. **b**, For prometaphase to late anaphase, the averaging domain is a 5 μm (x) by 5 μm (y) by 6 μm (z) cuboid. Spindles are aligned onto the *x*-*y* midplane ($z = 0$), at which plane the mean 2D projection vector field is plotted. And the purple frame (3D view) is the purple square frame in **a**. **c**, An exception for the PNC stage, the averaging cuboid measures 5 μm (x) by 5 μm (y) by 9 μm (z) (larger size in the *z* direction). The purple square in the upper panel is the purple frame (3D view) in the bottom panel. **d**,**e**, The simulated fluid flows (in the *x*-*y* plane of spindle motion) at the peak of the oscillations, time T_p, under (**d**) the cytoplasmic pulling or (**e**) the cortical pulling models. **f**, The experimental flow vector field derived from averaging the movements of tracked FNDs in 17 embryos at time T_p. **g**, Left, definition of pronuclear migration/centration and rotation progression. Middle, the averaged pronuclear experimental fluid data with migration ratio $R = 0.35 \sim 0.5$ (the same data as Fig. 5e). Right, the data with rotation angle $A = 33° \sim 66°$. For all experimental fluid data, the statistical significance of the velocity vectors is indicated by their colour scale (*P*-value colour bar) (see Methods for details). Arrows on centrosomes indicate mean measured centrosome velocities.

https://doi.org/10.1038/s41567-023-02223-z

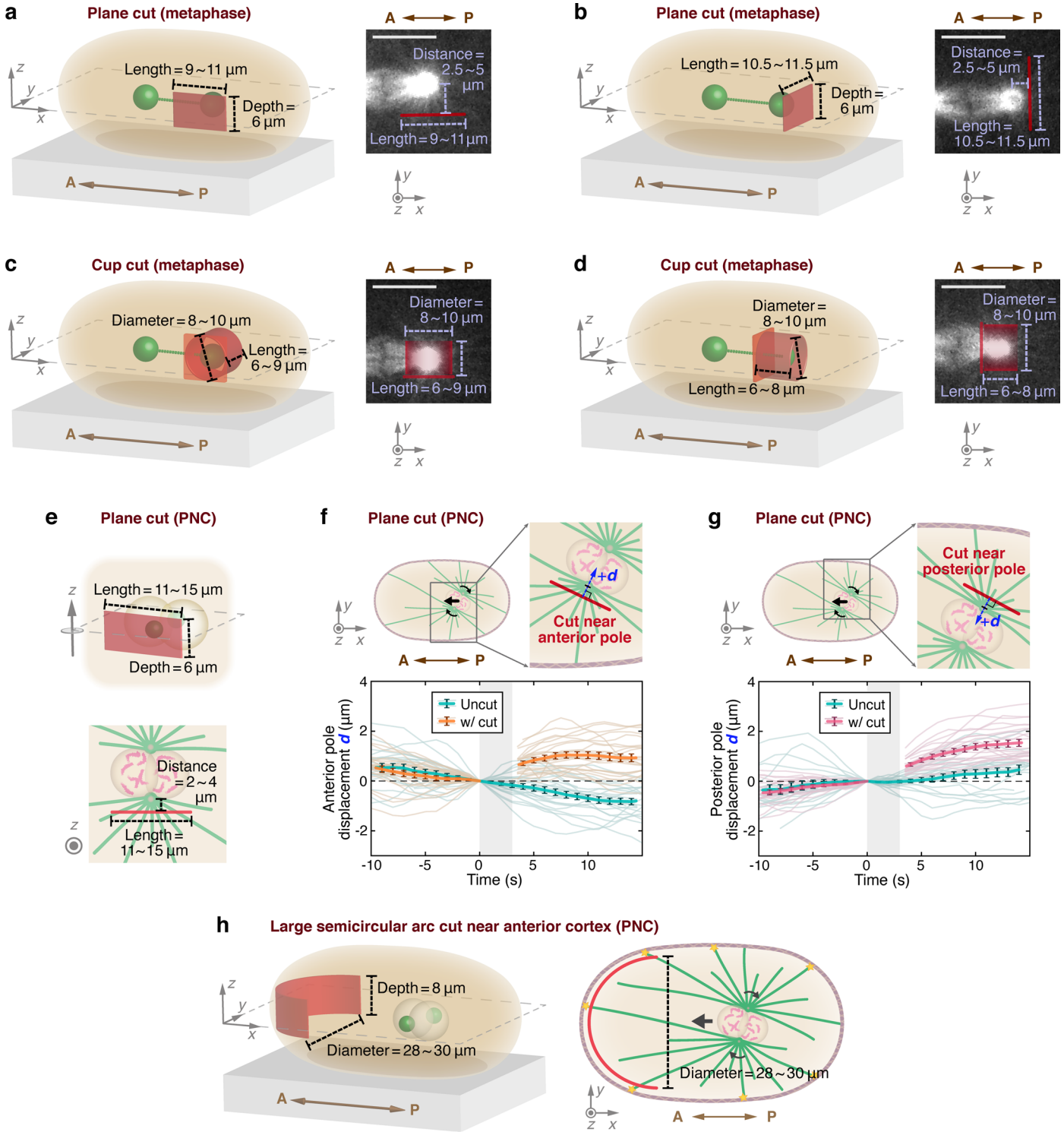

Extended Data Fig. 4 | Dimensions of laser ablation experiments performed in metaphase and the PNC stage. Centrosomes are presented by green balls in all 3D schematics. Centrosomes and astral MTs are sketched in green and chromosomes in magenta in all 2D schematics. All ablation geometrics are portrayed in red. The A–P directions are indicated by brown arrows. **a**,**b**, Metaphase: dimensions of the rectangular plane cuts in Fig. 4a,b respectively. **c**,**d**, Metaphase: dimensions of the cup cuts in Fig. 4c,d respectively. **e**, The PNC stage: dimensions of the rectangular plane cuts in Fig. 5a,b. **f**,**g**, The PNC stage: the plane cuts near the anterior or leading centrosomes (**f**), and the plane cuts near the posterior or trailing centrosomes (**g**). Both upper parts are the schematics showing the definition of centrosome centre displacement *d*, which is the relative orthogonal (away from the plane cut) displacement from the locus right before cutting. The black arrows indicate the progression of pronuclear migration and rotation. The mean displacement results with SEM error bars, including uncut and cut embryos, are shown in both lower parts. Their raw data are plotted semi-transparently in the back layer. Sample numbers are **f**, $n = 25$ (uncut), $n = 25$ (with cut) and **g**, $n = 23$ (uncut), $n = 23$ (with cut). And the data in Fig. 5b is the combination of these two data sets (**f** and **g**), including both plane cuts near the leading and the trailing centrosomes. **h**, The PNC stage: dimensions of the large semicircular arc cuts (near anterior cortices) in Fig. 5f–h. All scale bars on images are 10 μm.

https://doi.org/10.1038/s41567-023-02223-z

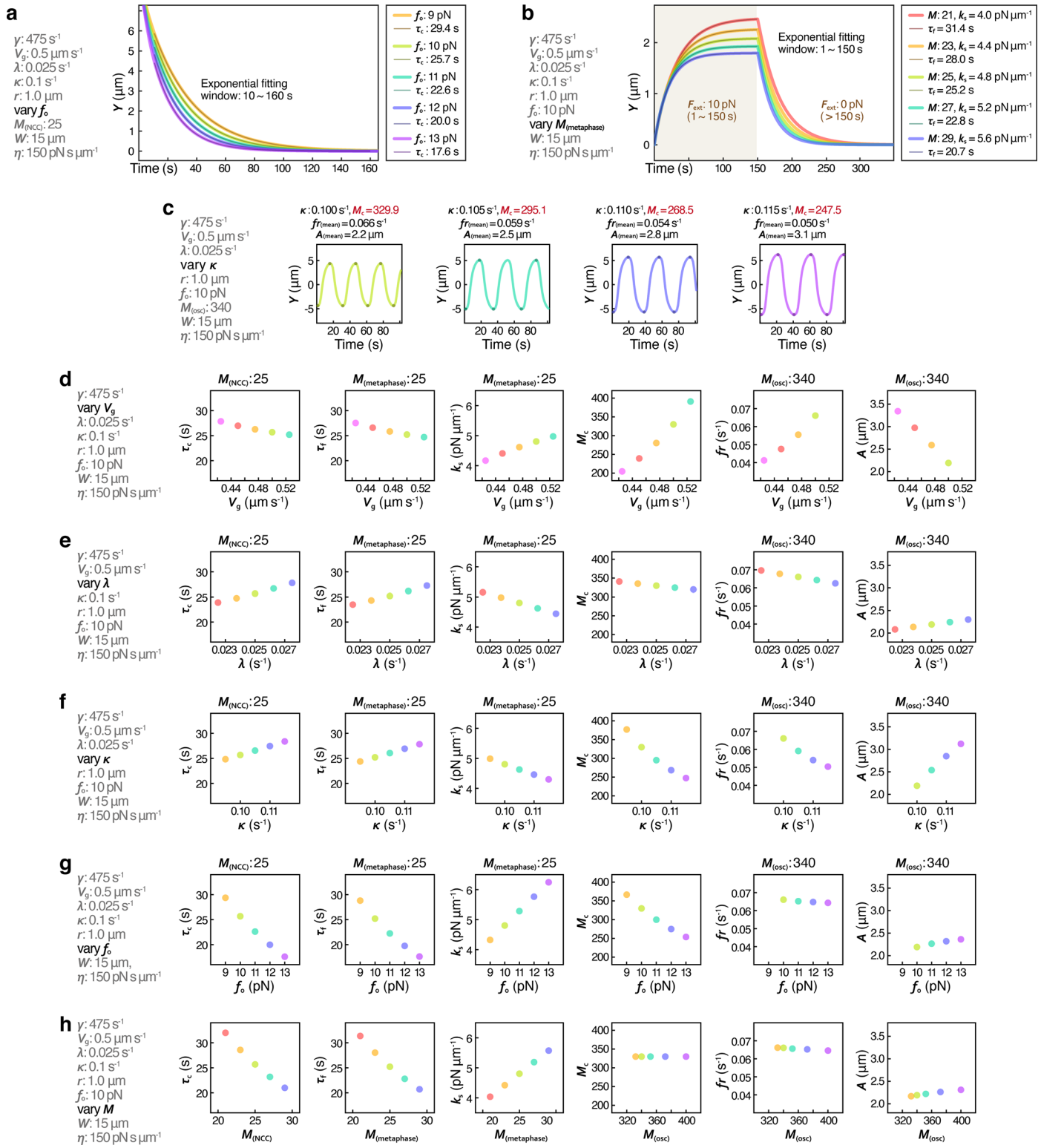

Extended Data Fig. 5 | Parameter sweeping simulations of the cortical pulling model. a-c, The examples of simulated centrosome movements while parameter sweeping. **a**, How varying the pulling force f_0 per force generator affects the PNC centration and the corresponding exponential fitting of τ_c. **b**, How varying the motor number M in metaphase affects the stable centring behavior under the condition of exerting an external force for 150 seconds and releasing. The centrosome motion is shown with the corresponding exponential fitting of τ_f and the spring constant k_s calculated from the theory. **c**, How changing the cortical motor detachment rate κ affects the spindle oscillations. The corresponding M_c were derived from the theory and we adopted the same motor number (above all M_c) to simulate the oscillations. The averaged oscillation frequencies and amplitudes are specified. **d-h**, The results of PNC centration (τ_c), metaphase stable centring (τ_f and spring constant k_s), and anaphase oscillation (M_c, and oscillation frequency and amplitude) under different parameters.

https://doi.org/10.1038/s41567-023-02223-z

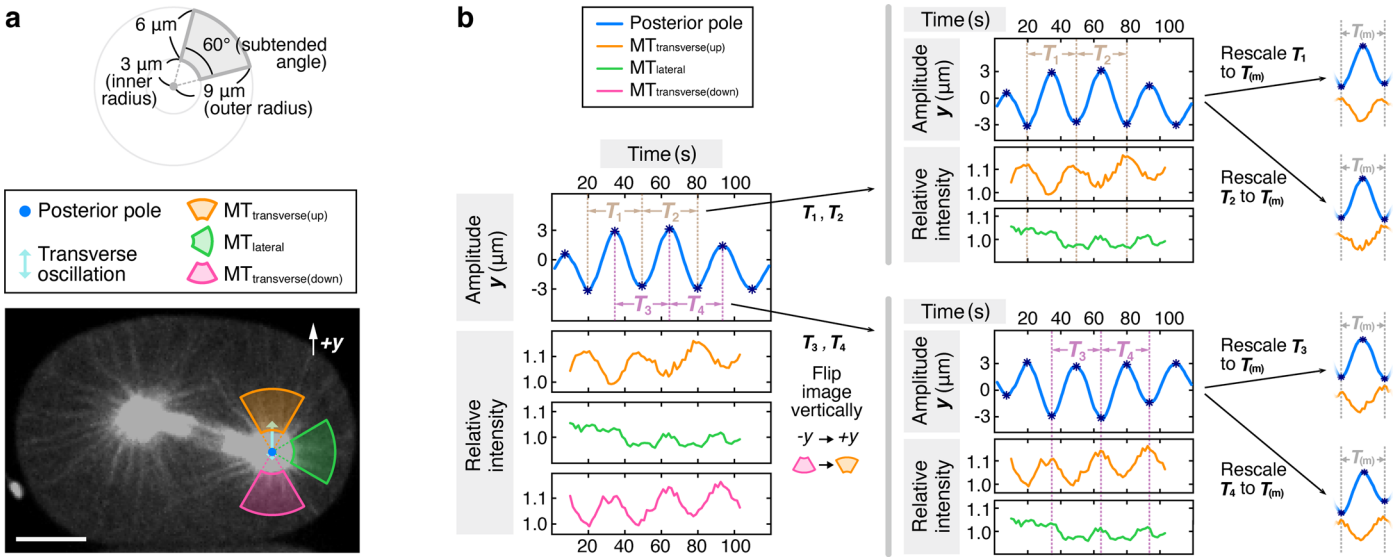

Extended Data Fig. 6 | Quantification of astral MTs intensity during transverse oscillations. a, One snapshot from the example GFP::β-tubulin time-series with the assigned transverse and lateral annular-sector regions shown (scale bar, 10 µm). The dimensions of the annular sectors are depicted on the top. **b**, Detailed information about data alignment for intensity measurement. Please refer to Methods for detailed operations.

https://doi.org/10.1038/s41567-023-02223-z

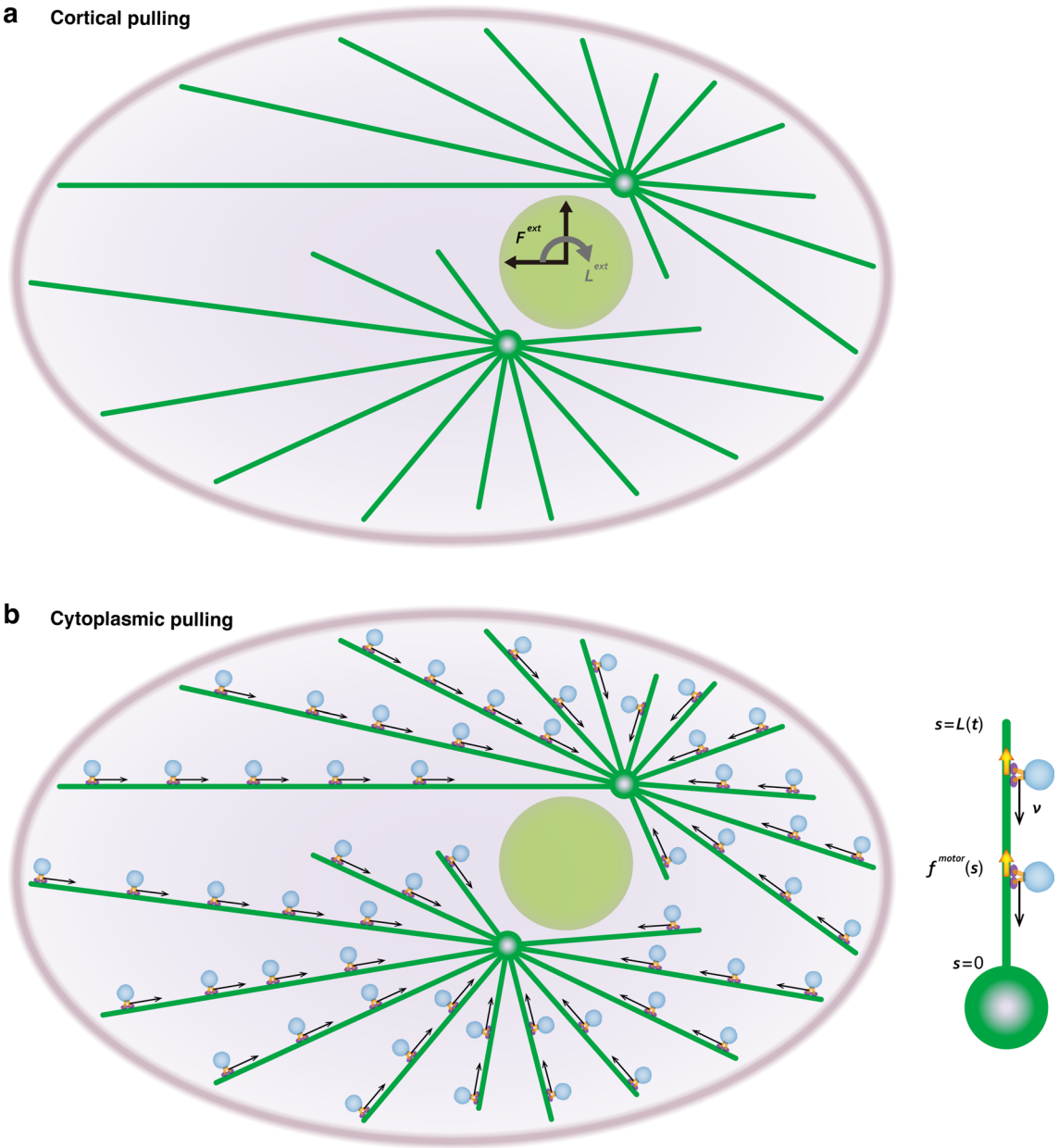

c

Initial (*x*,*y*) position values (μm)

Object \ Event	oscillation (T_m)	oscillation (T_p)	prometaphase	metaphase elongation	pronuclear migration
posterior centrosome	(12.7, 0)	(12.2, 1.7)	(6.2, 0.5)	(8.9, 0)	(7.3, 2.6)
spindle/pronuclei(PNC)	(3.3, -0.05)	(2.75, 0)	(0.8, 0)	(1.65, 0)	(3.7, 0)
anterior centrosome	(-6.1, -0.1)	(-6.7, -1.7)	(-4.6, -0.5)	(-5.6, 0)	(0.1, -2.6)

Extended Data Fig. 7 | Models of the force transduction mechanisms and initial position values in computational fluid dynamics simulations. **a**,**b**, Schematics for the computational models of the force transduction mechanisms. The figure shows the PNC stage (see Fig. 5e for the corresponding experiment). Our simulations have five structural elements: the cell cortex (gray purple ellipses), the spindle/pronuclei (light green circles), the centrosomes (green circles), elastic MTs (green lines) and the cytoplasm, the fluid filling inside the cortex. **a**, *Cortical pulling*. Due to the cortical pulling forces, MTs remain straight and the forces directly act on the PNC without any loss for the MT bending. Hence, in a short time horizon, the cytoplasmic flow arises from the translation and rotation of the pronuclei-centrosome- MT complex. We model that mechanism by applying an external force $\boldsymbol{F}^{ext}$ and torque $\boldsymbol{L}^{ext}$ on the PNC. **b**, *Cytoplasmic pulling*. Cytoplasmic dynein motors attach to the MTs and walk towards the centrosomes with velocity $\boldsymbol{v}$ (black arrow). As they do so, they apply a pulling force on the MTs in the opposite direction to their motion. We model the force applied by the motors by a continuum model: $\boldsymbol{f}^{motor}(s)$. **c**, The initial (x,y) positions (in μm) of the spindle's (or pronuclei's) and the centrosomes' centres in the simulations. All objects are at $z = 0$. We decided on those values based on the experiments (see Fig. 3e for oscillation, Fig. 4g for prometaphase, Fig. 4j for metaphase elongation, and Fig. 5e for the pronuclear migration).

https://doi.org/10.1038/s41567-023-02223-z

Extended Data Table 1 | Simulation parameters for the cortical pulling coarse-grained model

Simulation parameter	Value	References
spherical cell radius	15 [μm]	Estimated in this study.
microtubule growth rate (V_g)	0.5 [μm s^{-1}]	71
microtubule catastrophe rate (λ)	0.025 [s^{-1}]	46
microtubule nucleation rate (γ)	475 [s^{-1}]	72
microtubule-force-generator detachment rate (κ)	0.1 [s^{-1}]	53
force-generator capture radius (r)	1.0 [μm]	46, 51
force-generator pulling force (f_0)	10 [pN]	46
centrosome drag (η)	150 [pN s μm^{-1}]	16

nature physics

Article

https://doi.org/10.1038/s41567-023-02223-z

Laser ablation and fluid flows reveal the mechanism behind spindle and centrosome positioning

In the format provided by the authors and unedited

Supplementary Methods: computational fluid dynamics simulations

I) Numerical methods for computing intracellular flows

We give a brief description of the computational methods used to compute the cytoplasmic flow results shown in the main text. These methods were developed and applied originally to study the dynamics of pronuclear migration and centering [73, 74]. These methods, based upon boundary integral methods, slender-body theory, and fast Stokes equation solvers, account for the hydrodynamic interactions that couple together microtubules (MTs), any internal bodies (here, the spindle or pronuclear complex (PNC), and centrosomes) and the cell cortex. They also account for MT flexibility, dynamic instability, and MT interactions with molecular motors or boundaries.

The cell interior is treated as having five structural elements (See Extended Data Fig. 7a): the spindle body or pronuclei, the centrosomes, the cell cortex (boundary), the arrays of MTs nucleated from the centrosomes, and the cytoplasmic fluid. Given the slow speed and small scale of intracellular flows, any inertial effects can safely be ignored. While we assume the cytoplasm is itself a Newtonian fluid [16], the response of the MT-laden cytoplasmic system is non-Newtonian. The flow of a Newtonian cytoplasm is described by the incompressible Stokes equations:

$$\mu\Delta\boldsymbol{u} - \nabla p = \mathbf{0} \quad \& \quad \nabla \cdot \boldsymbol{u} = 0,$$

where μ is the cytoplasmic viscosity, $\boldsymbol{u}$ is the (cytoplasmic) fluid velocity, and p is the pressure which maintains flow incompressibility.

Solutions to the Stokes equations can be represented through boundary integral formulations [75], where the fluid velocity is represented as an integral distribution of fundamental solutions to the Stokes equations on all immersed and bounding surfaces. That is, for N MTs and M other immersed surfaces (cortex, centrosomes, …) we can represent these distributions in the form

$$\boldsymbol{u}(\boldsymbol{x}) = \sum_{i=1}^{M} \boldsymbol{u}_i^S(\boldsymbol{x}) \; + \; \sum_{m=1}^{N} \boldsymbol{u}_m^{MT}(\boldsymbol{x}) \, .$$

The densities of these distributions are determined and coupled together by the application of boundary conditions, such as the no-slip condition (surface velocity is equal to fluid velocity) or applied forces and torques. A boundary integral formulation reduces the computational problem from being three-dimensional (solving the Stokes equations in the fluid volume) to the two-dimensional problem of solving coupled singular integral equations on all the immersed and bounding surfaces.

Of particular interest here are MTs. MTs have a diameter of $a \approx 25$ nm and lengths of $L \sim 1$ - 20 μm, yielding small slenderness ratios of $\epsilon = 10^{-3}$ - 10^{-2}. This allows their flow contributions to be treated specially: their surface integrals can be reduced, through asymptotics, to line integrals of ''Stokeslet'' fundamental solutions along their centerlines [76, 77, 78]. In particular, to leading order in slenderness ratio, the induced fluid velocity from the m^{th} MT, having centerline coordinates $\boldsymbol{X}_m(s,t)$, with $s \in [0, L_m]$ the arclength from its minus end and L_m the MT length, is

$$\boldsymbol{u}_m^{MT}(\boldsymbol{x}) \; = \int_0^{L_m} \boldsymbol{S}\big(\boldsymbol{x} - \boldsymbol{X}_m(s')\big)\boldsymbol{f}_m(s') \, ds'.$$

Here the second-rank tensor $\boldsymbol{S}(\boldsymbol{r}) = (\boldsymbol{I} + \hat{\boldsymbol{r}}\hat{\boldsymbol{r}})/(8\pi\mu|\boldsymbol{r}|)$, with $\hat{\boldsymbol{r}} = \boldsymbol{r}/|\boldsymbol{r}|$, is the (single-layer) Stokeslet fundamental solution of the Stokes equations, and $\boldsymbol{f}_m$ is the force/length the MT exerts upon the fluid. To leading order, the velocity of the n^{th} MT centerline is given by

$$\frac{\partial \boldsymbol{X}_n}{\partial t}(s,t) = \sum_{i=1}^{M} \boldsymbol{u}_i^S(\boldsymbol{X}_n) + \sum_{m \neq n}^{N} \boldsymbol{u}_m^{MT}(\boldsymbol{X}_n) - \frac{\ln(\epsilon_n^2 e)}{8\pi\mu}\left(\boldsymbol{I} + \frac{\partial \boldsymbol{X}_n}{\partial s}\frac{\partial \boldsymbol{X}_n}{\partial s}\right)\boldsymbol{f}_n \, .$$

The force $\boldsymbol{f}_m$ arises from internal elastic forces, and from external forces either at MT ends (through boundary conditions), or along MT lengths. The internal elastic forces are related to MT conformation by Euler-Bernoulli beam theory using the constitutive relation $\boldsymbol{f} = -E\boldsymbol{X}_{ssss} + (T\boldsymbol{X}_s)_s$, with E the MT flexural modulus, and T is MT axial tension. The first term is the

bending force per unit length and the second is the tensile force per unit length. The tension T is determined by the condition of MT inextensibility [79].

MTs are nucleated from, and clamped rigidly to, centrosomes which are themselves mechanically coupled to the spindle or PNC. In our modeling, motion results from the application of forces and/or torques to these structural elements. The spatial discretization of all surfaces and MTs, application of quadrature formulae for surface integral equations, and the discretization in time of MT and body velocities results in a linear system of equations to be solved at each time-step to update all body positions and MT conformations. To solve this large system, we use the GMRES iterative solver [80] with a block-diagonal preconditioner [74]. Within this iterative method, we use a parallel implementation of the Kernel-Independent Fast Multipole Method [81] to hierarchically and efficiently evaluate all hydrodynamic interactions, leading to linear cost per time-step in the number of spatial unknowns (again, determined by the discretization of surfaces and MT center-lines).

I.i) Changes for the cytoplasmic pulling model.

In the cytoplasmic pulling model, cargo-carrying dyneins walk along MTs towards the centrosomes (MTs' minus ends) and so apply pulling forces on MTs (see Extended Data Fig. 7b). By Newton's third law of motion, the pulling forces on MTs are equal in magnitude and opposite in direction to the force that dynein exerts on the cytoplasm to drag the cargo through it. We treat the density of the attached dynein as a continuum field with constant number of attachments per unit length of MT, and the motor force as aligned along the MT. Thus, the pulling forces on a MT per unit length is $\boldsymbol{f}^{motor} = F_{dyn} n_{dyn} \boldsymbol{X}_s$ where F_{dyn} is the magnitude of the force applied from a single motor to a MT, n_{dyn} is the motor number density per unit length, and $\boldsymbol{X}_s$ is the tangent vector to the MT. Accordingly, we modify the dynamics equation for MT motion to

$$\frac{\partial \boldsymbol{X}_n}{\partial t}(s,t) = \sum_{i=1}^{M} \boldsymbol{u}_i^S(\boldsymbol{X}_n) + \sum_{m \neq n}^{N} \boldsymbol{u}_m^{MT}(\boldsymbol{X}_n) - \frac{\ln(\epsilon_n^2 e)}{8\pi\mu}\left(\boldsymbol{I} + \boldsymbol{X}_{n,s}\boldsymbol{X}_{n,s}\right)\left(\boldsymbol{f}_n + \boldsymbol{f}_n^{motor}\right).$$

However, for induced flows away from the MT, the pulling forces on MTs are balanced by the forces exerted on the cytoplasm to drag the cargo (i.e. the far-field motor-induced flow is from a dipolar force), and the dominant effect is that from the internal elastic force $\boldsymbol{f}_n$. Thus, the expression for $\boldsymbol{u}_m^{MT}(\boldsymbol{x})$ is unmodified [74, 82].

II) Simulation setups

We used the experimentally measured centrosome velocities of the spindle assembly at various stages to set the conditions of comparison with our simulations. In particular, we performed short time simulations, explicitly to recover the instantaneous cytoplasmic velocity fields induced by motion of the spindle/pronuclei-centrosome assembly and the attached MTs.

In the cortical pulling model (Extended Data Fig. 7a), previous studies of Nazockdast *et al* [73] show that MTs remain nearly straight under their extensile loading from cortically bound dynein motors. Hence, the cortical pulling forces directly act on the spindle/pronuclei-centrosome assembly without substantial loss to MT bending, which is equivalent to applying an external force and torque at the assembly's center. In this case, the cytoplasmic velocity arises from the translations and rotations of the spindle/pronuclei-centrosome-MT complex [73]. We implemented the cortical pulling mechanism by applying an external force and torque on the assembly which we adjusted to match the centrosome velocities in the experiments.

For the cytoplasmic pulling model, at short times as in our simulations, we find that the instantaneous velocities scale to a very good approximation with the magnitude of the applied pulling forces. Hence, we adjusted the motor force/length to match, in each case, the experimental centrosome velocities.

We also used experimentally measured positions and sizes of the spindle/pronuclei and centrosomes in the simulations (see Extended Data Fig. 7c). We modeled the centrosomes as rigid spheres of diameter 1 μm which, in most cases, were moved in a rigid frame with the

pronucleus or spindle body. Each centrosome had on the order of 300 attached MTs. This number is smaller than the actual number of astral MTs [72], however, by running the simulations for different numbers of MTs we found that the qualitative features remain similar.

Before starting the fluid dynamics simulations, we simulated MTs' dynamic instability with a MT catastrophe rate of 0.015 sec^{-1}, nucleation rate per centrosome of 62.5 sec^{-1} and MT growth velocity of 0.75 μm/sec. In particular, holding fixed the positions of the spindle/pronuclei and the centrosomes, we let MTs nucleate and grow from the centrosomes. Depolymerization occurred either through spontaneous catastrophe during free growth, or upon colliding with the cortex. After the MTs reached their steady-state length distribution (i.e., an exponential distribution truncated by catastrophe at the cortex), we activated either cortical or cytoplasmic pulling forces, depending upon the scenario. For each stage, we ran simulations for ten different initializations of MT arrays and presented averaged results over those samples.

II.i) Spindle in oscillation

At this stage, the spindle is modelled as a rigid ellipsoid of length 16.8 μm along the anterior-posterior axis (A-P axis), and of width 4 μm at the spindle center. The spindle was also slightly rotated in the counterclockwise direction (0.005 rad) because the anterior centrosome is below the A-P axis whereas the posterior one is upon it (see Fig. 3e). The centrosomes are constrained to move in the same rigid frame as the spindle.

Cytoplasmic pulling. The cytoplasmic pulling model does not lend itself straightforwardly to capturing the observed centrosome and spindle speeds, and so adjustments are necessary. During spindle oscillation the spindle center is shifted towards the posterior of the cell. Hence, in our modeling of the centrosomal array, the posterior centrosome has shorter MTs towards the posterior end than does the anterior centrosome towards the anterior (see Extended Data Fig. 7c). Loading the MTs uniformly with motors then leads the spindle-centrosome assembly to move towards the anterior. Additionally, both centrosomes are almost on the A-P axis (see Fig. 3e).

Thus, the centrosomes have MTs of similar lengths above and below their centers, which generates weaker flow in the axis perpendicular to the A-P axis than that along the A-P axis. So, to match the centrosomes' velocities, we varied the motor density across the MTs instead of having them uniformly distributed.

Cortical pulling. To capture the experimentally observed centrosome and spindle speeds, we applied forces in the x- and y-directions, and a torque in the z-direction, on the spindle-centrosome assembly.

II.ii) Spindle in prometaphase

We modeled the spindle in prometaphase as a sphere of 5 μm diameter. The experiment observations (see Fig. 4g) show negligible motion of the centrosomes or spindle at this stage.

Cytoplasmic pulling. Since there is not any reference velocity for us to scale the motor force/length, we used the same value for all the MTs which is the same as in the pronuclear migration simulations. Their symmetry produces no motion of the centrosomes, but considerable cytoplasmic motion.

Cortical pulling. It is assumed that the total pulling force upon the spindle-assembly was zero, which generates neither centrosome nor cytoplasmic motion.

II.iii) Spindle in metaphase elongation

The spindle was modelled as a rigid ellipsoid of 12.5 μm in length, and of 4 μm in width at the spindle center. We modeled the elongation of the spindle as a prescribed rate of increase in distance between the centrosomes, as measured experimentally, with the spindle body constrained to stay at their midpoint.

Cytoplasmic pulling. Again, this model requires some adaptation to achieve the experimentally observed centrosome velocities. Here, the motor force/length was the same for all the MTs which has the same magnitude as in the prometaphase and pronuclear migration simulations. But, it was taken as slightly greater on the posterior MTs so as to prevent the anterior centrosome from moving. Due to greater motor force/length on the posterior MTs, one could expect to see faster streaming velocity on the posterior. However, this is not observed because the posterior centrosome's motion in the x-direction drags fluid in the opposite direction to the flow the motor forces generate, and these counter-acting flows cancel each other near the posterior centrosome.

Cortical pulling. We let the centrosomes move as a result of the elongation of the spindle-centrosome complex along the A-P axis. Then, to reproduce the experimentally observed centrosome velocities, we applied a force on the spindle-centrosome assembly in the x-direction that canceled out the anterior centrosome's velocity.

II.iv) Pronuclear migration

We modeled the pronuclei as a rigid sphere of 5 μm diameter. The centrosomes were constrained to move in the same rigid frame as the pronuclei.

Cytoplasmic pulling. We used the same motor force/length for all the MTs, keeping it similar in magnitude to those used in the other simulations, but adjusting it to achieve the observed centrosome velocities.

Cortical pulling. To achieve the observed centrosome velocities, we applied a torque in the clockwise direction and a force with components in the anterior and y-directions.

II. v) Combining the pulling models

In the both cortical and cytoplasmic pulling models (Extended Data Fig. 7), previous studies of Nazockdast *et al* [73] show that MTs remain nearly straight under their extensile loading by

dynein motors. Hence, in our computations here, again, we take the MTs to be straight for both models and so contributions from bending forces are absent. The consequent velocity field will then be that for a rigid structure of MTs, centrosomes, and PNC or spindle. That velocity field is then found through solution of linear equations for MT tension T, and the surface vector density $\mathbf{q}$ of the double-layer integrals that captures the velocity contributions from the immersed surfaces of the centrosomes, PNC/spindle, and cortex [73].

For the cortical pulling model these equations can be written in the form

$$\mathcal{H}_1[T_{cort}] + \mathcal{L}_1[\mathbf{q}_{cort}] = \begin{bmatrix} \mathbf{F} \\ \tau \end{bmatrix}$$

$$\mathcal{H}_2[T_{cort}] + \mathcal{L}_2[\mathbf{q}_{cort}] = \mathbf{0}$$

where $\mathbf{F}$ and τ are the applied force and torque, and $\mathcal{H}_{1,2}$ and $\mathcal{L}_{1,2}$ are linear integral and differential operators acting along MTs and all surfaces. For the cytoplasmic fulling model the equations instead have the form

$$\mathcal{H}_1[T_{cyto}] + \mathcal{L}_1[\mathbf{q}_{cyto}] = \begin{bmatrix} 0 \\ 0 \end{bmatrix}$$

$$\mathcal{H}_2[T_{cyto}] + \mathcal{L}_2[\mathbf{q}_{cyto}] = \mathbf{f}_m$$

where $\mathbf{f}_m$ is comprised of the vectors $f_m \mathbf{X}_m$ of motor forcing. Note that in either case that if $\mathbf{F} = \tau = \mathbf{0}$, or $\mathbf{f}_m = 0$, then the tension and density will both be zero.

Given a tension T, and a density $\mathbf{q}$, the cytoplasmic velocity can generally be expressed as

$$\mathbf{u}(\mathbf{x}) = \mathcal{M}[T] + \mathcal{N}[\mathbf{q}]$$

Where $\mathcal{M}$ and $\mathcal{N}$ are again linear integral and differential operators. Now, if instead we consider a mixed model, with contributions from both cortical and cytoplasmic pulling, of the form

$$\mathcal{H}_1[T_{mix}] + \mathcal{L}_1[\mathbf{q}_{mix}] = \alpha \begin{bmatrix} \mathbf{F} \\ \tau \end{bmatrix}$$

$$\mathcal{H}_2[T_{mix}] + \mathcal{L}_2[\mathbf{q}_{mix}] = \beta\, \mathbf{f}_m$$

then $T_{mix} = \alpha T_{cort} + \beta T_{cyto}$ and $\mathbf{q}_{mix} = \alpha \mathbf{q}_{cort} + \beta \mathbf{q}_{cyto}$ is its solution. Hence, the induced cytoplasmic velocity, using linearity, is

$$\mathbf{u}(\mathbf{x}) = \alpha \mathcal{M}[T_{cort}] + \beta \mathcal{M}[T_{cyto}] + \alpha \mathcal{N}[\mathbf{q}_{cort}] + \beta \mathcal{N}[\mathbf{q}_{cyto}]$$

$$= \alpha \mathbf{u}_{cort}(\mathbf{x}) + \beta \mathbf{u}_{cyto}(\mathbf{x})$$

that is, is a linear combination of both cortical and cytoplasmic pulling models. As a verification on our code, we have directly checked this property of a mixed pulling model.

Supplementary Notes: coarse-grained model of cortical pulling

Here we derive a coarse-grained model of a centrosome moving in a spherical cell, subject to pulling forces from force generators on the cell surface. We start by considering an isolated centrosome nucleating microtubules (MTs) that undergo dynamic instability (*section I*). We then construct a model of stoichiometric force generators in which each force generator can bind to at most one MT at a time (*section II*). We show that pulling forces from stoichiometric force generators are sufficient to stably position the centrosome or produce oscillations (even in the absence of additional forces from MT pushing or bending). We next construct a model of non-stoichiometric force generators in which force generators bind all MTs that contact them (*section III*). We show that pulling forces from non-stoichiometric force generators are always destabilizing and cannot stably position the centrosome.

I) Nucleation and growth of microtubules (MTs) from a centrosome

We consider a centrosome with MTs nucleating with equal probability in all directions with rate γ, which then grow with velocity V_g and undergo catastrophe with rate λ. The length distribution of MTs, $\psi(l,t)$, satisfies the Fokker-Planck equation:

$$\partial_t \psi(l,t) + V_g \partial_l \psi(l,t) = -\lambda \psi(l,t)$$

Setting the flux $V_g\psi$ at $l = 0$ to be equal to the nucleation rate gives $V_g\psi(0,t) = \gamma$, or $\psi(0,t) = \gamma/V_g$. Starting from an initial state with no MTs present (i.e. $\psi(l > 0{,}0) = 0$), the complete time-dependent solution for the length distribution of MTs is

$$\psi(l,t) = \frac{\gamma}{V_g} e^{-l\lambda/V_g} \Theta\left(l - V_g t\right)$$

where $\Theta(a) = 1$ for $a \leq 0$ and $\Theta(a) = 0$ for $a > 0$. Thus, there is a front of MTs propagating outwards at a speed V_g. No MTs extend beyond the front, while MTs behind the front have a (truncated) exponential length distribution. At long times, this approaches the steady state MT length distribution $\psi(l) = \frac{\gamma}{V_g} e^{-l\lambda/V_g}$.

The total number of MTs, $N_{MT}(t)$, is given by $N_{MT}(t) = \int_0^\infty \psi(l,t)\, dl$, which, for an unconfined centrosome at steady-state, becomes $N_{MT} = \int_0^\infty \psi(l)\, dl = \int_0^\infty \frac{\gamma}{V_g} e^{-l\lambda/V_g}\, dl = \gamma/\lambda$.

II) Stoichiometric force generators

II.i) An individual stoichiometric force generator: Here we derive a model for stoichiometric force generators, in which each force generator can bind to at most one MT at a time. An unbound force generator will bind to a MT that contacts it, while a bound force generator detaches from the MT it is associated with at rate κ. When the force generator is bound to a MT, it exerts a pulling force on the centrosome of $f_0\hat{\boldsymbol{\xi}}$, where $\hat{\boldsymbol{\xi}}$ is the unit vector pointing from the centrosome to the force-generator (Fig. 6b). Thus, the expected force that the force generator exerts on the centrosome at time t is $\vec{\boldsymbol{f}}_{fg}(t) = f_0 P(t)\hat{\boldsymbol{\xi}}$, where $P(t)$ is the probability that the force generator is bound to a MT at time t. $P(t)$, in turn, obeys the dynamics

$$\dot{P}(t) = \Omega(t)(1 - P(t)) - \kappa P(t)$$

Where $\Omega(t)$ is the rate at which MTs impinge upon the force generator at time t. We next calculate $\Omega(t)$.

MT impingement rate: We calculate the rate that growing MTs impinge upon a disk-shaped force-generator of radius r, located a distance d away from a centrosome at the origin. Only MTs located in a cone defined by the position of the centrosome and the projected area of the force-generator can grow to contact the force-generator. The number of MTs located in this cone is (approximately)

$$N(t) = \int_0^{\vartheta_m} \frac{\sin\vartheta}{2} d\vartheta \int_0^d \psi\,(l,t) dl = \chi(d) \int_0^d \psi\,(l,t) dl$$

where $\vartheta_m = \tan^{-1}(r/d)$ is the solid angle of the cone and $\chi(d) = \frac{1}{2}\left(1 - \frac{1}{\sqrt{1+(r/d)^2}}\right)$ is the fraction of MTs nucleated from the centrosome that fall inside the cone.

For the moment we shall assume that growing MTs are impinging directly upon the force generator, i.e. that $\psi(d,t) > 0$, and that the centrosome is moving at speeds slower than V_g. The time derivative of the number of MTs inside the cone is then

$$\dot{N}(t) = \gamma\chi(d) - \lambda N(t) + \frac{\chi'(d)}{\chi(d)} \dot{d} N(t) - \left(V_g - \dot{d}\right)\chi(d)\psi(d,t)$$

The first term is gain from nucleation and the second term is loss from catastrophes. The third term is change from the cone getting wider or narrower from changes in *d*. The last term is a loss term from MTs hitting the force generator at the cone end, a distance d from the centrosome. If the centrosome is moving with speed $V_{cen} = -\dot{d}$, either directly away from or to the force generator, then the rate of impingement of MTs is given by

$$\Omega(t) = \left(V_{cen} + V_g\right)\chi(d)\psi(d,t)$$

and since, by assumption, $|V_{cen}| < V_g$, this rate is always positive. More generally, if the centrosome is moving with velocity $\vec{\boldsymbol{V}}_{cen}$, then the plus ends of MTs in the cone move with net velocity $\vec{\boldsymbol{V}} = \vec{\boldsymbol{V}}_{cen} + V_g\hat{\boldsymbol{\xi}}$, and the rate of impingement of MTs on the force generator is

$$\Omega(t) = \left(\vec{\boldsymbol{V}} \cdot \hat{\boldsymbol{n}}\right)\chi(d)\psi(d,t)$$

where $\hat{\boldsymbol{n}}$ is an outward unit vector normal to the surface of the force generator. At any time $t > d/V_g$, after the onset of nucleation, one can assume that $\psi(d,t) = \frac{\gamma}{V_g}e^{-d\lambda/V_g}$.

In this model, MTs grow until they hit the cell boundary at which point they either bind to an unoccupied force generator, or disassemble. If the centrosome moves away from the force generator at speeds greater than V_g (i.e. $\vec{\boldsymbol{V}} \cdot \hat{\boldsymbol{n}} < 0$), then the growing MT plus ends will have a net velocity that also causes them to move away from the force generator, and hence the rate of impingement $\Omega(t)$ of these MTs onto the force generator will be zero. As described in *section I*, these MTs will form a free front of plus-ends growing away from the centrosome at speed V_g. The evolution of that front, and determining when it reattaches to the boundary, becomes part of the full dynamics and is discussed in *section II.v* on nonlinear dynamics.

II.ii) Net pulling force in a spherical cell with stoichiometric force generators: We next calculate the net pulling force acting on a centrosome in a spherical cell of radius W with M stoichiometric force generators uniformly spread over the cell surface (Fig. 6b, right). We consider a centrosome moving along the y-axis, located at position $Y(t)$, moving with velocity $\vec{\boldsymbol{V}}_{cen} = \dot{Y}(t)\hat{\boldsymbol{y}}$. Again, for the moment we assume that the centrosome is moving at speeds slower than V_g.

The net force acting on the centrosome is obtained by summing the force from all M force generators, each located at position $\vec{\boldsymbol{x}}_i$

$$\vec{\boldsymbol{F}}_{fg} = \sum_i^M \vec{\boldsymbol{f}}_{fg}(\vec{\boldsymbol{x}}_i) = \sum_i^M f_0 P(\vec{\boldsymbol{x}}_i, t)\hat{\boldsymbol{\xi}}(\vec{\boldsymbol{x}}_i)$$

To make further progress, we coarse-grain by approximating the sum over discrete force generator positions by an integral over all positions on the surface of the sphere (which is equivalent to assuming a continuum of force generators, uniformly covering the sphere)

$$\vec{\boldsymbol{F}}_{fg} \approx \frac{Mf_0}{4\pi W^2}\int_{|\vec{\boldsymbol{x}}|=W} dS_x P(\vec{\boldsymbol{x}}, t)\hat{\boldsymbol{\xi}}(\vec{\boldsymbol{x}})$$

We assume symmetry about the y-axis and parameterize the location of the force generators by the polar angle φ (Fig. 6b). A force generator at angle φ on the surface of the cell is located at position $\vec{\boldsymbol{x}} = W\hat{\boldsymbol{n}}(\varphi)$, where $\hat{\boldsymbol{n}}(\varphi) = \sin\varphi\,\hat{\boldsymbol{x}} + \cos\varphi\,\hat{\boldsymbol{y}}$ is the unit vector normal to the surface of that force generator. The vector from the centrosome to the force generator is $W\hat{\boldsymbol{n}}(\varphi) - Y(t)\,\hat{\boldsymbol{y}}$, so the unit vector pointing from the centrosome to the force-generator is $\hat{\boldsymbol{\xi}}(\varphi) = (W\hat{\boldsymbol{n}}(\varphi) - Y(t)\,\hat{\boldsymbol{y}})/d(\varphi)$. The distance from the centrosome to the force generator is $d(\varphi) = \sqrt{W^2 - 2WY\cos\varphi + Y^2}$. Thus, the MT plus ends move at velocity $\vec{\boldsymbol{V}} = \dot{Y}(t)\hat{\boldsymbol{y}} + V_g\hat{\boldsymbol{\xi}}(\varphi)$, and the projection of the MT plus end velocity onto the direction of the force generator is $\vec{\boldsymbol{V}}\cdot\hat{\boldsymbol{n}}(\varphi) = \dot{Y}\cos\varphi + \frac{V_g}{d(\varphi)}(W - Y\cos\varphi)$.

Then, projecting the net pulling force in the $\hat{\boldsymbol{y}}$ direction gives

$$F_{fg} = \frac{Mf_0}{2}\int_0^\pi d\varphi \sin\varphi\;\hat{\boldsymbol{\xi}}(\varphi)\cdot\hat{\boldsymbol{y}}\,P(\varphi)$$

$$= \frac{Mf_0}{2}\int_0^\pi d\varphi \sin\varphi\;\frac{W}{\sqrt{W^2 - 2WY\cos\varphi + Y^2}}\left(\cos\varphi - \frac{Y}{W}\right)P(\varphi)$$

II.iii) Equations of motion with stoichiometric force generators: In addition to pulling forces from the force-generators, we also consider the drag on the centrosomes, $F_{drag} = -\eta\dot{Y}$, with drag coefficient η, which accounts for the drag of both the centrosome itself and the associated astral microtubule array. From force-balance, $F_{drag} + F_{fg} = 0$, which gives

$$\dot{Y} = \frac{Mf_0}{2\eta}\int_0^{\pi} d\varphi \sin\varphi \, \frac{W}{\sqrt{W^2 - 2WY\cos\varphi + Y^2}} \left(\cos\varphi - \frac{Y}{W}\right) P(\varphi) \quad [\mathbf{1}]$$

The equations of motion for the system consist of two coupled equations, the force-balance equation [**1**] for $\dot{Y}$, and the dynamical equation for P:

$$\partial_t P(\varphi) = \Omega\big(\dot{Y}, Y, \varphi\big)\big(1 - P(\varphi)\big) - \kappa P(\varphi) \qquad [\mathbf{2}]$$

where

$$\Omega\big(\dot{Y}, Y, \varphi\big) = \big(\vec{\boldsymbol{V}} \cdot \hat{\boldsymbol{n}}\big)\chi(d)\psi(d)$$
$$= \left(\dot{Y}\cos\varphi + \frac{V_g W - V_g Y\cos\varphi}{d}\right) \cdot \frac{1}{2}\left(1 - \frac{1}{\sqrt{1 + (r/d)^2}}\right) \cdot \frac{\gamma}{V_g} e^{-d\lambda/V_g} \quad [\mathbf{3}]$$

is the impingement rate, and

$$d = d(Y, \varphi) = \sqrt{W^2 - 2WY\cos\varphi + Y^2}$$

II.iv) Centered steady-state and its stability with stoichiometric force generators: At steady-state, $\dot{Y} = 0$ and $\dot{P} = 0$, which results when the centrosome is at the center of the sphere, with steady-state position $\bar{Y} = 0$, and steady-state attachment probability

$$\bar{P} = \frac{\bar{\Omega}}{\bar{\Omega} + \kappa}$$

Where the steady-state rate of impingement of MTs onto the surface of the sphere is

$$\bar{\Omega} = V_g \chi(W)\psi(W) = \frac{1}{2}\left(1 - \frac{1}{\sqrt{1 + (r/W)^2}}\right)\gamma e^{-W\lambda/V_g} \approx \frac{\gamma}{4}\left(\frac{r}{W}\right)^2 e^{-W\lambda/V_g}$$

We next investigate the stability of the centered state by considering small perturbations: i.e. $Y = \bar{Y} + \varepsilon\tilde{Y}(t) = \varepsilon\tilde{Y}(t)$ and $P = \bar{P} + \varepsilon\tilde{P}(\varphi, t)$ for $\varepsilon \ll 1$. Inserting the perturbations into the equations for $\dot{Y}$ and $\dot{P}$, retaining only the leading-order $O(\varepsilon)$ terms, and integrating the $\dot{P}$ equation against $\sin\varphi\cos\varphi$, yields two ODEs:

$$\dot{\tilde{Y}} = \frac{Mf_0}{2\eta}\tilde{P}_{\langle\varphi\rangle} - \frac{2}{3}\frac{\bar{P}Mf_0}{W\eta}\tilde{Y} \quad \text{and} \quad \dot{\tilde{P}}_{\langle\varphi\rangle} = \frac{2}{3}\frac{\kappa\bar{P}B}{W}\tilde{Y} + \frac{2}{3}\frac{\kappa\bar{P}}{V_g}\dot{\tilde{Y}} - \frac{\bar{\Omega}}{\bar{P}}\tilde{P}_{\langle\varphi\rangle}$$

Where $\tilde{P}_{\langle\varphi\rangle} = \tilde{P}_{\langle\varphi\rangle}(t) = \int_0^\pi d\varphi \sin\varphi \cos\varphi \, \tilde{P}(\varphi, t)$ and $B = \frac{W\lambda}{V_g} + \frac{r}{W}\frac{\chi\prime(W)}{\chi(W)} \approx \frac{W\lambda}{V_g} + 2$

with $\chi(W) = \frac{1}{2}\left(1 - \frac{1}{\sqrt{1+(r/W)^2}}\right)$ and $\chi'(W) = \frac{r/W}{2[1+(r/W)^2]^{3/2}}$.

The approximate expression for B omits terms of order $\left(\frac{r}{W}\right)^2$, which can be safely neglected because the force-generators are substantially smaller than the cell in all cases of interest. Taking a time derivative of the $\dot{\tilde{Y}}$ equation, and substituting back in the $\dot{\tilde{P}}_{\langle\varphi\rangle}$ equation, leads to a single second-order ODE for this system:

$$\ddot{\tilde{Y}} + \left[\frac{Mf_0\bar{P}}{3\eta V_g W}\left(2V_g - \kappa W\right) + \frac{\bar{\Omega}}{\bar{P}}\right]\dot{\tilde{Y}} + \left[\frac{2Mf_0}{3\eta W}\left(\bar{\Omega} - \frac{\kappa\bar{P}B}{2}\right)\right]\tilde{Y} = 0$$

We search for solutions of the form $\tilde{Y} \propto e^{\sigma t}$, yielding

$$\sigma^2 + \left[\frac{Mf_0\bar{P}}{3\eta V_g W}\left(2V_g - \kappa W\right) + \frac{\bar{\Omega}}{\bar{P}}\right]\sigma + \frac{2Mf_0}{3\eta W}\left(\bar{\Omega} - \frac{\kappa\bar{P}B}{2}\right) = 0$$

This gives two roots. If the real parts of both roots are negative, then the centrosome will stably position in the center of the cell. Starting from stable centering, we consider two ways to lose stability: 1) if both roots remain real, but one becomes positive, then the centrosome will tend to spontaneously decenter; 2) if both roots become purely imaginary, then the centrosome undergoes a Hopf bifurcation to an oscillatory state. We next perform a more detailed examination of three cases –spontaneous decentering, oscillations, and stable centering.

Spontaneous decentering: If $\bar{\Omega} < \frac{\kappa\bar{P}B}{2}$ then both roots are real, and at least one of them is positive. Under this scenario, the centrosome will tend to spontaneously decenter. This criterion can be roughly interpreted as stating that the center will lose stability if the rate that unbound motors become bound, $\sim\bar{\Omega}$, becomes less than the rate that bound motors unbind MTs, $\sim\kappa\bar{P}$. The inequality can be approximated as $\frac{\gamma}{4}\left(\frac{r}{W}\right)^2 e^{-W\lambda/V_g} < \frac{\kappa W\lambda}{2V_g}$. Thus, the center becomes unstable

when the nucleation rate, γ, size of the force generators, r, or average MT length, V_g/λ, becomes too small; when the size of the cell, W, increases too much; or when the detachment rate, κ, becomes too large. Note, that in the case considered here, of non-interacting force generators, the criterion for spontaneous decentering is independent of M, the number of force generators. Thus, the centrosome can remain stably positioned with arbitrarily more force generators than MTs, demonstrating that the stability of the center is not due to a "limiting number" of force generators.

Oscillations: When $\bar{\Omega} = \frac{Mf_0}{3\eta V_g W}\left(\kappa W - 2V_g\right)\bar{P}^2$ the eigenvalues are purely imaginary, i.e. $\sigma = \pm\sigma_c = \pm i\omega_c$, which indicates oscillatory behavior. Passing from the stable centering regime, described above, through this point to an oscillatory state is a loss of stability via a Hopf bifurcation. This Hopf bifurcation can only occurs if $\frac{1}{\kappa} < \frac{W}{2V_g}$, i.e. only if the time a MT stays attached to a force generator is sufficiently small compared to the time it takes for a MT to grow across the cell. In that case, increasing motor number causes such a transition from stable centering to oscillations at a critical number of motors

$$M_c = \frac{3\eta\bar{\Omega}}{f_0\bar{P}^2}\frac{V_g W}{\left(\kappa W - 2V_g\right)} = \frac{3\eta(\bar{\Omega}+\kappa)^2}{f_0\bar{\Omega}}\frac{V_g W}{\left(\kappa W - 2V_g\right)}$$

with a frequency

$$\omega_c^2 = \frac{2}{3}\frac{M_c f_0}{W\eta}\left(\bar{\Omega} - \frac{\kappa\bar{P}B}{2}\right) \approx \frac{2}{3}\frac{M_c f_0}{W\eta}\bar{P}\bar{\Omega} = \frac{\bar{\Omega}(\bar{\Omega}+\kappa)}{\left(\frac{\kappa W}{2V_g} - 1\right)} \approx \frac{2V_g}{W}\bar{\Omega}\left(1 + \frac{\bar{\Omega}}{\kappa}\right)$$

Stable centering: The centrosome is stable in the center position if the real parts of both roots are negative. This occurs when the rate at which MT impinge upon the cell surface is sufficiently high. Specifically, it requires that

$$\bar{\Omega} > \frac{Mf_0}{3\eta V_g W}\left(\kappa W - 2V_g\right)\bar{P}^2 \text{ and } \bar{\Omega} > \frac{\kappa\bar{P}B}{2}$$

When the centrosome is stably positioned at the cell center, it is natural to ask how it responds to an externally applied force. Force-balance then becomes $F_{drag} + F_{fg} + F_{ext} = 0$. Taking the external force to be small, $F_{ext} = \varepsilon f_{ext}$, and expanding to linear order yields

$$\ddot{\tilde{Y}} + \left[\frac{Mf_0\bar{P}}{3\eta V_g W}\left(2V_g - \kappa W\right) + \frac{\bar{\Omega}}{\bar{P}}\right]\dot{\tilde{Y}} + \left[\frac{2}{3}\frac{Mf_0}{\eta W}\left(\bar{\Omega} - \frac{\kappa\bar{P}B}{2}\right)\right]\tilde{Y} = \frac{\bar{\Omega}}{\eta\bar{P}}f_{ext} + \frac{1}{\eta}\dot{f}_{ext}$$

Note that the response of the centrosome to an applied force is not equivalent to a spring-and-dashpot model because the additional degree of freedom associated with motor attachments makes the dynamics of $\tilde{Y}$ contain a second derivative with respect to time and explicitly dependent on the rate of change of the applied force (i.e. it is a second order system with numerator dynamics). However, at steady-state, this becomes

$$\frac{2}{3}\frac{Mf_0}{W}\frac{\bar{P}}{\bar{\Omega}}\left(\bar{\Omega} - \frac{\kappa\bar{P}B}{2}\right)\tilde{Y} = f_{ext}$$

Thus, at steady-state, the displacement, $\tilde{Y}$, varies linearly with the applied force, like a spring, with spring-constant

$$k_s = \frac{2}{3}\frac{Mf_0}{W}\frac{\bar{P}}{\bar{\Omega}}\left(\bar{\Omega} - \frac{\kappa\bar{P}B}{2}\right) \approx \frac{2}{3}\frac{Mf_0}{W}\bar{P}^2$$

If the center position is stable then, $\bar{\Omega} > \frac{\kappa\bar{P}B}{2}$, and thus $k_s > 0$, as expected. Note that the spring constant is roughly the average number of engaged force generators, $M\bar{P}$, times the average force per force generator, $f_0\bar{P}$, divided by the width of the cell, W.

If the centrosome is displaced from the center (or if it starts off center), then it will move to the cell center. After a quick initial transient, the approach to the center will be exponential, with a time scale, τ_c, given by

$$\frac{1}{\tau_c} = \frac{1}{2}(\bar{\Omega} + \kappa)\left(1 - \frac{M}{M_c}\right)$$

This same time-scale dominates in the response to an applied force. Note that a naïve guess for τ_c would be the spring constant, k_s, divided by the drag coefficient, η, as would result from a simple spring and dashpot mechanical model. However, in our model, based on the biophysics of

MTs and molecular motors, τ_c is not simply related to the spring constant, but rather depends on processes such as MT detachment rate and polymerization dynamics.

II.v) Non-linear dynamics with stoichiometric force generators: We next consider the full non-linear, time-dependent behavior of a centrosome in a spherical cell with stoichiometric cortical force generators (including allowing for centrosome speeds greater than V_g). As described in *section I*, the full time-dependent solution of $\psi(l,t)$ contains a front of MTs propagating outwards at a speed V_g. If this front of leading MT plus-ends is not in contact with a force generator, then $\Omega(t)$, the impingement rate of MTs upon that force generator, is zero. If the front does contact the force generator, then the impingement rate is given by the value calculated in *section II.i*. With this procedure for determining $\Omega(t)$, we numerically solve the equations of motion for $\dot{Y}$ and $\dot{P}$ given in *section II.iii*, while numerically tracking the front of leading MT plus-ends.

We describe the front of leading MT plus-ends in terms of a coordinate system centered on the centrosome with polar angle φ'. There is a one-to-one mapping between this coordinate system and the coordinate system used to describe the position of the motors, which is centered on the cell center with polar angle φ. Thus, we can write $\varphi = \varphi(\varphi', t)$. We assume that the centrosomal array does not rotate, and represent the location of the plus-end front as $\vec{\boldsymbol{S}}(\varphi', t) = Y(t)\hat{\boldsymbol{y}} + D(\varphi', t)\hat{\boldsymbol{e}}(\varphi')$, where $\hat{\boldsymbol{e}}(\varphi') = (\cos\varphi', \sin\varphi')$ and $D(\varphi', t)$ is the distance from the centrosome to the front. The front is in one of two states; either

(i) the front is at the cortex, i.e. $D(\varphi', t) = d(\varphi(\varphi', t), t)$. So, MTs are impinging on force generators, which implies $\Omega(\varphi(\varphi', t), t) > 0$; or

(ii) the front is short of, and growing towards, the cortex, i.e. $D(\varphi', t) < d(\varphi(\varphi', t), t)$ and $\partial_t D(\varphi', t) = V_g$. So, MTs are not impinging on force generators, which implies $\Omega(\varphi(\varphi', t), t) = 0$.

Moreover, the front remains in contact with the cortex, i.e. in state (i), only so long as the centrosome is not moving away faster than V_g.

We numerically track the front through a first-order time-stepping framework: Initial data Y^0, $P^0(\varphi)$, and $D^0(\varphi')$ are specified. Then,

1. given a time-step Δt, and $(Y^n,\ P^n, D^n, \Omega^n)$ (and hence d^n) at time $t^n = n\Delta t$, find Y^{n+1} and P^{n+1} at time $t^{n+1} = (n+1)\Delta t$ using Euler's method for the equations of motion for $\dot{Y}$ and $\dot{P}$ given in *section II.iii*.

2. Let $\widetilde{D}(\varphi') = D^n(\varphi') + \Delta t V_g$; Given Y^{n+1} determine the mappings $\varphi = \varphi(\varphi', t^{n+1})$ and its inverse $\varphi' = \varphi'(\varphi, t^{n+1})$, and $d^{n+1}(\varphi)$.

3. Update D and Ω according to the following scheme:

If $\widetilde{D}(\varphi') \geq d^{n+1}(\varphi(\varphi', t^{n+1}))$

$D^{n+1}(\varphi') = d^{n+1}(\varphi(\varphi', t^{n+1}))$

$\Omega^{n+1}\big(\varphi(\varphi', t^{n+1})\big) = \left[\vec{V}^{n+1} \cdot \hat{n}\right]_+ \chi(d^{n+1})\psi(d^{n+1})$,

with $\psi(d) = \frac{\gamma}{V_g} e^{-d\lambda/V_g}$

else $(\widetilde{D}(\varphi') < d^{n+1}(\varphi(\varphi', t^{n+1})))$

$D^{n+1}(\varphi') = \widetilde{D}(\varphi')$

$\Omega^{n+1}\big(\varphi(\varphi', t^{n+1})\big) = 0$

this completes one time-step.

III) Non-stoichiometric force generators

III.i) An individual non-stoichiometric force generator: Here we derive a model for non-stoichiometric force generators, in which any MT that contacts a force-generator is subject to pulling forces, even if that force-generator is already pulling on other MTs. An MT that contacts

a force generator binds to it, while bound MTs detach from force generators at rate κ. Every MT bound to the force generator is subject to a pulling force $f_0\hat{\boldsymbol{\xi}}$, where $\hat{\boldsymbol{\xi}}$ is the unit vector pointing from the centrosome to the force-generator (Fig. 6b). Thus, the force that the force generator exerts on the centrosome at time t is $\vec{\boldsymbol{f}}_{fg}(t) = f_0 m(t)\hat{\boldsymbol{\xi}}$, where $m(t)$ is the number of MTs bound to the force generator at time t. The expected value of $m(t)$, in turn, obeys the dynamics

$$\dot{m}(t) = \Omega(t) - \kappa m(t)$$

where $\Omega(t)$ is the rate at which MTs impinge upon the force generator at time t. As derived in *section II.ii*,

$$\Omega(t) = \left[\vec{\boldsymbol{V}} \cdot \hat{\boldsymbol{n}}\right]_+ \chi(d)\psi(d,t)$$

Here $[a]_+ = a$ for $a > 0$ and zero otherwise, and its appearance here reflects the fact that MTs will not reach the force generator if the centrosome is moving away faster than the MT growth speed. $\hat{\boldsymbol{n}}$ is a unit vector normal to the surface of the force generator, d is the distance between the force generator and the centrosome, and the net velocity of the plus ends of MTs is $\vec{\boldsymbol{V}} = \vec{\boldsymbol{V}}_{cen} + V_g\hat{\boldsymbol{\xi}}$ (where $\vec{\boldsymbol{V}}_{cen}$ is the velocity of the centrosome).

III.ii) Net pulling force in a spherical cell with non-stoichiometric force generators: We next calculate the net pulling force acting on a centrosome in a spherical cell of radius W with M non-stoichiometric force generators uniformly spread over the cell surface (Fig. 6b). We consider a centrosome moving along the y-axis, located at position $Y(t)$, moving with velocity $\vec{\boldsymbol{V}}_{cen} = \dot{Y}(t)\hat{\boldsymbol{y}}$. The net force acting on the centrosome is obtained by summing the force from all M force generators, each located at position $\vec{\boldsymbol{x}}_i$

$$\vec{\boldsymbol{F}}_{fg} = \sum_i^M \vec{\boldsymbol{f}}_{fg}(\vec{\boldsymbol{x}}_i) = \sum_i^M f_0 m(\vec{\boldsymbol{x}}_i, t)\hat{\boldsymbol{\xi}}\,(\vec{\boldsymbol{x}}_i)$$

To make further progress, we coarse-grain by approximating the sum over discrete force generator positions by an integral over all positions on the surface of the sphere (which is equivalent to assuming a continuum of force generators, uniformly covering the sphere)

$$\vec{\boldsymbol{F}}_{fg} \approx \frac{Mf_0}{4\pi W^2}\int_{|\vec{\boldsymbol{x}}|=W} dS_x m(\vec{\boldsymbol{x}},t)\hat{\vec{\boldsymbol{\xi}}}(\vec{\boldsymbol{x}})$$

Projecting this net pulling force in the $\hat{\boldsymbol{y}}$ direction, and using the geometry described in *section II.ii* gives

$$F_{fg} = \frac{Mf_0}{2}\int_0^{\pi} d\varphi \sin\varphi\, \hat{\vec{\boldsymbol{\xi}}}(\varphi)\cdot\hat{\boldsymbol{y}}\, m(\varphi)$$

$$= \frac{Mf_0}{2}\int_0^{\pi} d\varphi \sin\varphi\, \frac{W}{\sqrt{W^2 - 2WY\cos\varphi + Y^2}}\left(\cos\varphi - \frac{Y}{W}\right) m(\varphi)$$

III.iii) Equations of motion with non-stoichiometric force generators: In addition to pulling forces from the force-generators, we also consider the drag on the centrosomes, $F_{drag} = -\eta\dot{Y}$, with drag coefficient η. From force-balance, $F_{drag} + F_{fg} = 0$, which gives

$$\dot{Y} = \frac{Mf_0}{2\eta}\int_0^{\pi} d\varphi \sin\varphi\, \frac{W}{\sqrt{W^2 - 2WY\cos\varphi + Y^2}}\left(\cos\varphi - \frac{Y}{W}\right) m(\varphi)$$

The equations of motion of the system consist of three coupled equations, this force-balance equation for $\dot{Y}$, the dynamical equation for $\dot{m}$, and the evolution equation for the MT length distribution, ψ:

$$\partial_t m(\varphi) = \Omega\left(\dot{Y}, Y, \varphi\right) - \kappa m(\varphi)$$

$$\partial_t \psi(\varphi, l) + V_g \partial_l \psi(\varphi, l) = -\lambda\psi(\varphi, l)$$

where the MT length distribution, ψ, can vary with angle around the centrosome. $\psi(0,t) = \gamma/V_g$ and ψ is coupled to the boundary by the condition that MTs do not grow past the cell surface. m is coupled to ψ through the rate of impingement of MTs

$$\Omega\left(\dot{Y}, Y, \varphi\right) = \left[\vec{V}\cdot\hat{n}\right]_+ \chi(d)\psi(\varphi, d)$$

$$= \left[\dot{Y}\cos\varphi + \frac{V_g W - V_g Y\cos\varphi}{\sqrt{W^2 - 2YW\cos\varphi + Y^2}}\right]_+ \frac{1}{2}\left(1 - \frac{1}{\sqrt{1 + (r/d)^2}}\right)\psi(\varphi, d)$$

and

$$d = d(Y, \varphi) = \sqrt{W^2 - 2WY\cos\varphi + Y^2}$$

III.iv) Steady-state and stability with non-stoichiometric force generators: At steady-state, $\dot{Y} = 0$ and $\dot{m} = 0$, which results when the centrosome is at the center of the sphere, with steady-state position $\bar{Y} = 0$, and steady-state number of attached MTs per force generator $\bar{m} = \frac{\bar{\Omega}}{\kappa}$. Where the steady-state rate of impingement of MTs onto the surface of the sphere is

$$\bar{\Omega} = V_g \chi(W)\psi(W) = \frac{1}{2}\left(1 - \frac{1}{\sqrt{1 + (r/W)^2}}\right)\gamma e^{-W\lambda/V_g} \approx \frac{\gamma}{4}\left(\frac{r}{W}\right)^2 e^{-W\lambda/V_g}$$

We next investigate the stability of the centered state by considering small perturbations: i.e. $Y = \bar{Y} + \varepsilon\tilde{Y}(t) = \varepsilon\tilde{Y}(t)$ and $m = \bar{m} + \varepsilon\tilde{m}(\varphi, t)$ for $\varepsilon \ll 1$. Inserting the perturbations into the equations for $\dot{Y}$ and $\dot{m}$, retaining only the leading-order $O(\varepsilon)$ terms, and integrating the $\dot{m}$ equation against $\sin\varphi\cos\varphi$, yields two ODEs:

$$\dot{\tilde{Y}} = \frac{Mf_0}{2\eta}\tilde{m}_{\langle\varphi\rangle} - \frac{2}{3}\frac{\bar{\Omega}Mf_0}{\kappa W\eta}\tilde{Y} \text{ and } \quad \dot{\tilde{m}}_{\langle\varphi\rangle} = \frac{2}{3}\frac{\bar{\Omega}B}{W}\tilde{Y} + \frac{2}{3}\frac{\bar{\Omega}}{V_g}\dot{\tilde{Y}} - \kappa\tilde{m}_{\langle\varphi\rangle}$$

Where $\tilde{m}_{\langle\varphi\rangle} = \tilde{m}_{\langle\varphi\rangle}(t) = \int_0^\pi d\varphi \sin\varphi\cos\varphi\,\tilde{m}(\varphi, t)$ and $B = \frac{W\lambda}{V_g} + \frac{r}{W^2}\frac{\chi'(W)}{\chi(W)} \approx \frac{W\lambda}{V_g} + 2$. The approximate expression for B omits terms of order $\left(\frac{r}{W}\right)^2$, which can be safely neglected because the force-generators are substantially smaller than the cell in all cases of interest. Taking a time derivative of the $\dot{\tilde{Y}}$ equation, and substituting back in the $\dot{\tilde{m}}_{\langle\varphi\rangle}$ equation, leads to a single second-order ODE for this system:

$$\ddot{\tilde{Y}} + \left[\frac{Mf_0\bar{\Omega}}{3W\eta V_g\kappa}\left(2V_g - \kappa W\right) + \kappa\right]\dot{\tilde{Y}} + \left[\frac{Mf_0\bar{\Omega}}{3W\eta}(2 - B)\right]\tilde{Y} = 0$$

We search for solutions of the form $\tilde{Y} \propto e^{\sigma t}$, yielding

$$\sigma^2 + \left[\frac{Mf_0\bar{\Omega}}{3W\eta V_g\kappa}\left(2V_g - \kappa W\right) + \kappa\right]\sigma + \frac{Mf_0\bar{\Omega}}{3W\eta}(2 - B) = 0$$

This gives two roots. Note that since $B > 2$, one of the roots is always positive: i.e. small perturbations will grow and the center position is generically unstable. Thus, non-stoichiometric force generators produce pulling forces that are destabilizing. In contrast, pulling forces from stoichiometric force generators can result in stable centering (see *section II.iv*).

References

(References from Main Article)

16. Garzon-Coral C, Fantana HA, Howard J. A force-generating machinery maintains the spindle at the cell center during mitosis. *Science* 2016, **352**(6289)**:** 1124-1127.

72. Redemann S, Baumgart J, Lindow N, Shelley M, Nazockdast E, Kratz A*, et al.* C. elegans chromosomes connect to centrosomes by anchoring into the spindle network. *Nature communications* 2017, **8**(1)**:** 1-13.

(Supplementary Information-only References)

73. Nazockdast E, Rahimian A, Needleman D, Shelley M. Cytoplasmic flows as signatures for the mechanics of mitotic positioning. *Mol Biol Cell* 2017, **28**(23)**:** 3261-3270.

74. Nazockdast E, Rahimian A, Zorin D, Shelley M. A fast platform for simulating semi-flexible fiber suspensions applied to cell mechanics. *Journal of Computational Physics* 2017, **329:** 173-209.

75. Pozrikidis C. *Boundary integral and singularity methods for linearized viscous flow*. Cambridge University Press, 1992.

76. Götz T. *Interactions of fibers and flow: asymptotics, theory and numerics*. dissertation. de, 2001.

77. Johnson RE. An improved slender-body theory for Stokes flow. *Journal of Fluid Mechanics* 1980, **99**(2)**:** 411-431.

78. Keller JB, Rubinow SI. Slender-body theory for slow viscous flow. *Journal of Fluid Mechanics* 1976, **75**(4)**:** 705-714.

79. Tornberg A-K, Shelley MJ. Simulating the dynamics and interactions of flexible fibers in Stokes flows. *Journal of Computational Physics* 2004, **196**(1)**:** 8-40.

80. Saad Y, Schultz MH. GMRES: A generalized minimal residual algorithm for solving nonsymmetric linear systems. *SIAM Journal on scientific and statistical computing* 1986, **7**(3)**:** 856-869.

81. Malhotra D, Biros G. PVFMM: A parallel kernel independent FMM for particle and volume potentials. *Communications in Computational Physics* 2015, **18**(3)**:** 808-830.

82. Stein DB, De Canio G, Lauga E, Shelley MJ, Goldstein RE. Swirling Instability of the Microtubule Cytoskeleton. *Physical Review Letters* 2021, **126**(2)**:** 028103.